Multiphysics anti-icing simulation of a CFRP composite wing structure embedded with thin etched-foil electrothermal heating films in glaze ice conditions

Rene Roy[a], Lawrence Prince Raj[b], Je-Hyun Jo[c], Min-Young Cho[c], Jin-Hwe Kweon [a,c], Rho Shin Myong[a,c*]

[a] Research Center for Aircraft Core Technology, Gyeongsang National University, Jinju, Gyeongsangnam-do 52828, South Korea

[b] Aerospace Engineering and Applied Mechanics, Indian Institute of Engineering Science and Technology, Shibpur, Howrah 711103, India

[c] School of Mechanical and Aerospace Engineering, Gyeongsang National University, Jinju, Gyeongsangnam-do 52828, South Korea

E-mails: rroy@gnu.ac.kr (R Roy), lpraero@gmail.com (LP Raj), jjh0804@gnu.ac.kr (JH Jo), alsdud0540@gmail.com (MY Cho), jhkweon@gnu.ac.kr (JH Kweon), myong@gnu.ac.kr (RS Myong). (* Corresponding author)

Abstract

Electrothermal ice protection systems (IPS) for CFRP composite aircraft face distinct challenges because of the composite structure's relatively low thermal conductivity and vulnerability to overheating. In this work, the thermal response of a thin etched-foil heating film-based IPS integrated into CFRP laminates was characterized both experimentally and by thermal FEM simulation. A resulting IPS configuration was implemented in a CFRP wing skin laminate model of an unmanned aerial vehicle (UAV) for multiphysics icing simulation. Glaze ice accretion and melting were simulated with in-flight conditions and varying heater heat fluxes and angles of attack. Sharp surface temperature drops were observed in the heating film gap regions, which led to the implementation of a quasi-continuous film spacing. A uniform heater heat flux of 7.5 kW/m^2 achieved anti-icing functionality with an associated surface temperature range of 0–13°C. This range revealed the merit of heat flux zone modulation to uniformly distribute the surface temperature and improve the overall energy efficiency of the system.

Keywords: Aircraft anti-icing; Carbon fiber composite; Thermal properties; Thin films; Multiphysics simulation

1. Introduction

The widespread use of carbon fiber reinforced polymer (CFRP) composites in aircraft structures has prompted the development of anti- and de-icing methods specifically for these materials. CFRP has relatively lower thermal conductivity and is more vulnerable to overheating than traditional aluminum, so anti-icing systems must be carefully designed, or new anti-icing strategies developed. Anti-icing methods prevent ice buildup on the protected surface, either by evaporating the impinging water or by allowing it to run back and freeze on non-critical areas. Ice has a greater probability of forming on aircraft surfaces under certain flight and atmospheric conditions, which are referred to as *icing conditions* [1]. Ice build-up on aircraft surfaces can dangerously compromise flight safety, and thus aviation regulations specify that an aircraft must be equipped with an ice protection system (IPS) that is proven capable of maintaining safe flight operation in specified icing conditions [2].

Gaining a proper understanding of icing and IPS technology is still a current concern. For example, it was concluded that the root cause of the June 1st, 2009 Air France flight 447 fatal crash was ice crystal accumulation in a pitot probe [3]. For the anti-icing certification of pitot probes following the JAR 25 certification standard protocol [4], the Airbus SE company chose to apply an additional design margin coefficient factor of 2 to a specification of atmospheric water concentration. There is also evidence that icing certification for helicopters can be critical because of the potential for ice buildup on the engine air intake, and this can involve a comprehensive and expensive test program [5,6].

To assist IPS design and help reduce costs and development time, multiphysics icing simulation has been developed in recent

years. Here multiphysics generally refers to the simultaneous treatment of a wet dynamic airflow over a body, the accumulation of water droplets on the body's surface, heat transfer between solids and fluids, and the phase change of the water (icing). The thermal energy exchange between solids (conduction) and fluids (convection) can be directly modeled by conjugate heat transfer (CHT). This method has been validated, for example, using the software FENSAP-ICE and by icing wind tunnel testing of a rotorcraft engine air intake [7,8].

Common examples of existing aircraft IPS are based on i) turbine engine hot bleed air, ii) pneumatic boot inflation, iii) structure vibration, impulse or deformation, and iv) electrothermal heating elements [9–11]. It has been argued that hot bleed air IPS is not optimal for CFRP structures because of their low thermal conductivity and vulnerability to overheating [12]. Pneumatic boot inflation and structure impulse systems have limited anti-icing capability as they need a minimum thickness of ice buildup to function [13–15]. In contrast, electrothermal IPS is based on the Joule heating principle and can be digitally controlled to precisely heat-up specific aircraft surfaces. They are generally lightweight and require less infrastructure provided the aircraft is already equipped with an electrical source. The electrothermal process has highly efficient electrical power to heat conversion, although there is the obvious constraint of IPS power consumption, which is a net power expenditure for the aircraft [16,17].

Various forms of electrothermal IPS have been developed for composite structures in the past [12,18–28], as listed in Table 1. The heating methods can be classified as follows: i) resistance heating elements, ii) embedded conductive material networks, and iii) conductive coatings. Conductive material circuits placed next to the CFRP need to be electrically isolated, typically with glass fiber reinforced polymer (GFRP) plies or polymer layers. For aircraft applications (Fig. 1 (a) and (b)), the IPS also needs to be configured in relation to the actual geometry (e.g., curved wing shape), and also under realistic in-flight icing conditions (ambient temperature, cloud liquid water content, mean volume diameter of water droplets, and airspeed). Airspeed and ambient temperature in particular play a crucial role in the type of ice accretions formed on the aircraft surface and their impact on flight safety. So-called glaze ice is formed at high airspeeds and not-very-low ambient temperatures, when water droplets deform and/or flow along the surface prior to freezing. In contrast, rime ice is formed at low airspeeds and very low temperatures, when water droplets freeze immediately upon impact.

Table 1: Literature review of electrothermal IPS in composite structures.

| References	Heating Method (zoning)	Structure (material)	Airspeed [m/sec.]	Temperature [°C]	Liquid Water Content [g/m³]
De Rosa et al. (2011) [18]	Nichrome thin foil resistance (single-zone)	Curved wing skin (CFRP/GFRP)	63.8	-20	0.6
Mohseni et al. (2013) [19]	Constantan alloy wires (11–19 wires)	Curved wing skin (GFRP)	27.7	-17	0.84–1.05
Chu et al. (2014) [20]	Carbon nanotube paper (single-zone)	Plate (GFRP)	14	-22	3 mm ice cover
Falzon et al. (2015) [21]	Conductive carbon textile (single-zone)	Plate (CFRP)	0	-20	2.5 mm ice cover
Kim et al. (2016) [22]	Short carbon fiber mat (single-zone)	Plate (CFRP)	0	25	0 (dry)
Glover et al. (2017) [23]	Graphene ink coating (single-zone)	Plate (CFRP)	0	-15	2 mm ice cover
Laroche (2017) [24]	Constantan alloy wire, carbon fiber tow, CNT buckypaper (single-zone)	Plate (GFRP)	15	-10	0.5
Karim et al. (2018) [25]	Graphene ink-coated fibers (single-zone)	Plate (GFRP)	0	-1	Covered by ice cubes
Zhao et al. (2018) [26]	MWCNT-acrylic coating (single-zone)	Plate, propeller (GFRP)	10	-43	2.0
Yao et al. (2018) [12]	CNT forest (single-zone)	Plate (CFRP/GFRP)	0	-25	3 mm ice cover
Liu et al. (2019) [27]	MWCNT porous coating (single-zone)	Plate (GFRP)	10	-48	2.0
Ibrahim et al. (2019) [28]	3D-printed nichrome wires (dual-zone)	Plate (CFRP)	0	-17	Artic sea environment
Present work	Thin etched-foil films (1–15 zones)	Curved wing skin (CFRP)	102	-6.65	0.78
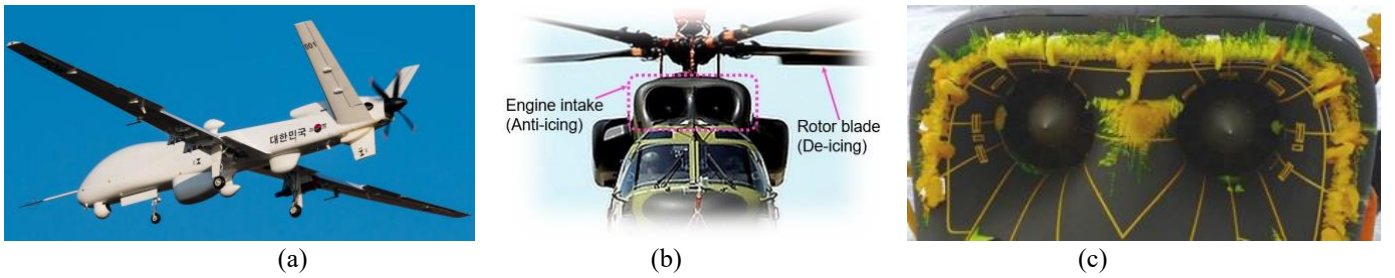
Figure 1: Examples of aircraft IPS applications: (a) Korean unmanned system (KUS-FS) medium-altitude long-endurance unmanned aerial vehicle (MALE-UAV); (b) Engine intake and rotor blades of the KAI KUH-1 Surion helicopter; (c) Result of in-flight icing testing of the helicopter engine air intake equipped with an electrothermal heat mat-based IPS.

Glaze ice is far more critical to aircraft safety, since it tends to run back along the airframe and can take more dangerous shapes, such as horn-ice. For this reason, we investigated glaze ice conditions — for example, at a high speed of 102 m/sec and a relatively warm temperature of –6.65°C. These values are in sharp contrast to previous work on rime ice conditions, in ranges of 0−63.8 m/sec and -48°C to -10°C, as shown in Table 1.

Fig. 1 (c) shows the actual results of in-flight icing testing of a helicopter engine air intake equipped with an electrothermal heat mat-based IPS. Accretions of yellow-dyed glaze ice indicate that the IPS needs to be modified to provide a greater heat load and wider coverage area on the engine intake. In general, the IPS should be able to effectively handle the large variations in local airflow conditions that occur around an aircraft. Because of this varying local airflow and the associated variations in surface heat transfer, the ability to independently modulate IPS in distinct zones (i.e., zoning) is clearly advantageous for improving overall energy efficiency.

Since in-flight icing is such a critical issue for safe aircraft operation, it is essential to accurately evaluate the performance of CFRP-based IPS in real in-flight icing conditions. Wet icing wind tunnel testing can be used, but the laboratory testing of scaled-down models introduces very complicated scaling laws, which are needed to determine collection efficiencies of water droplets and ice shapes, and as a result it cannot handle all of the meteorological icing conditions prescribed by an icing certification envelope [29]. Multiphysics icing simulation — the only method capable of exploring the full icing envelope — has been increasingly employed to predict ice accretion shapes for the design of ice protection systems [1,7].

High fidelity multiphysics icing simulations can help expand the scope of CFRP-based IPS analysis by directly addressing realistic in-flight conditions, including glaze ice conditions. Limited research has so far been reported on polymer composite IPS multiphysics icing simulation. Some have involved a GFRP structure with electrothermal heaters [30]. *Against this background, the aim of the present work is to evaluate the functionality of an electrothermal IPS for an CFRP aircraft wing structure under glaze ice conditions, using multiphysics icing simulation.*

We selected thin etched-foil electrothermal heating films to develop an IPS for carbon/epoxy prepreg-based CFRP composite laminates. Thin heating films have been applied for the anti-icing of aircraft windshields, for example, with an Indium Tin Oxide (ITO) film on the KAI KUH-1 Surion helicopter. However, as far as the authors are aware, they have never been applied to an aircraft composite structure. As a case application we chose an unmanned aerial vehicle (UAV) with a 1 mm thick CFRP laminate wing skin structure. A CFRP-based IPS structure was modeled in multiphysics icing simulation under glaze ice conditions with various angles of attack and IPS power inputs. Emphasis was placed on the application of thin etched-foil electrothermal IPS to CFRP structure to gain insights on the pertinent system characteristics, such as adequate surface temperature profile and the heat flux needed to achieve anti-icing. The study of these characteristics provides information on the requirements of CFRP-based electrothermal IPS for aircraft applications.

2. IPS design and laminate testing

2.1 Design parameters

As a case application we chose an IPS for the wing leading edge of a group 3 unmanned aerial vehicle (UAV) (weighing more than 55 lb, but less than 1320 lb). This application was chosen because there is currently considerable interest in this type of aircraft, and its scale is compatible with the heating films selected for this study. The representative flight conditions for this UAV are an aircraft speed of 128.6 m/sec and an altitude of 5500 meters [31]. The leading edge of the CFRP skin of this vehicle has a thickness on the order of 1 mm. We used carbon/epoxy unidirectional lamina prepreg to build 8-ply multi-angle laminates (USN125-B, SK chemicals, Seongnam, South Korea [32,33]). An aluminum foil cover (1100-H19 alloy) was also used, as it usually acts as an erosion shield [34]. Corkboard material was evaluated as a thermal insulator for the interior surface of the airfoil skin. The aluminum foil and corkboard materials were in some instances adhered to the CFRP with room temperature epoxy adhesive paste (Loctite EA 9394 AERO, Henkel Corporation Aerospace, Bay Point, USA [35]). The relevant material properties are listed in Table 2.

Table 2: IPS materials properties.

Material	Property	Symbol	Value
USN-125B carbon/epoxy prepreg unidirectional lamina [32,33,36,37]	Young's modulus	E_1	131 GPa
		E_2	7.6 GPa
	Shear modulus	G_{12}	5.34 GPa
	Poisson's ratio	v_{12}	0.31
	Cured ply thickness	t_{ply}	0.12 mm
	Thermal conductivity	$k_1{}^a$	10.5 W/(m·°C)
	Thermal conductivity	$k_2{}^b$	0.95 W/(m·°C)
	Thermal conductivity	$k_3{}^c$	0.95 W/(m·°C)
	Surface emissivity	ε	0.70
	Specific heat capacity	C_p	929 J/(kg·°C)
	Density	ρ	1.55 g/cm^3
Aluminum foil 1100-H19 [38,39]	Thermal conductivity	k	218 W/(m·°C)
	Surface emissivity	ε	0.25
	Specific heat capacity	C_p	904 J/(kg·°C)
	Density	ρ	2.70 g/cm^3
Corkboard [40,41]	Thermal conductivity	k	0.043 W/(m·°C)
	Surface emissivity	ε	0.93
	Specific heat capacity	C_p	1900 J/(kg·°C)
	Density	ρ	0.13 g/cm^3
Polyimide [42]	Thermal conductivity	k	0.12 W/(m·°C)
	Specific heat capacity	C_p	1090 J/(kg·°C)
	Density	ρ	1.42 g/cm^3
Epoxy adhesive paste [35]	Thermal conductivity	k	0.33 W/(m·°C)
	Specific heat capacity	C_p	1000 J/(kg·°C)
	Density	ρ	1.36 g/cm^3

[a]: parallel to fiber. [b]: perpendicular to fiber, lamina in-plane direction. [c]: lamina out-of-plane direction.

The CFRP thermal conductivity coefficients are based on test values published by Pilling and colleagues [36]. We chose to set the maximum heating film operating temperature at 70°C. Even though ice has a melting temperature close to 0°C for a wide range of practical pressures [43], in in-flight cold airflows cooling energy transfer can be significant, and even melted ice runback water can re-freeze at a downstream location if the wing skin surface is not kept hot enough [44,45]. A relatively higher temperature limit also enables the use of short-term high surface temperatures to rapidly melt any accreted ice. It is common for epoxy composites to have their maximum service temperature set at a 30°C margin below the material's glass transition temperature (T_g) [46]. In our case, the CFRP has a T_g of 125°C, so the 70°C maximum represents a safe 55°C margin below T_g.

2.2 Heating film power capacity sizing

We calculated the power capacity requirement of the heating films using a one-dimensional heat transfer analysis. The target parameter was to achieve the chosen 70°C maximum heating film temperature under all flight conditions. We considered an 8-ply laminate with a nominal thickness of 0.96 mm and an integrated heating film as a direct replacement of an area of lamina ply. In a simple model of a flat plate in a parallel flow, it can be assumed that the flow velocity will vary from zero (still air) to around the maximum flight velocity of 128.6 m/sec. Therefore we considered two limit cases: 1) in still air at sea level and -40°C, and 2) at 128.6 m/sec and 5500m altitude with a corresponding temperature of -55°C. For the still air case, the surface heat transfer coefficients were set as 5 W/(m²·K) [47]. For the maximum velocity case, we considered average surface convection heat transfer coefficients calculated from empirical correlations for both laminar and turbulent conditions [39]. The one-dimensional heat transfer calculation method is detailed in Appendix A. The calculated required heating film heat flux was 1.10 kW/m² in still air, 16.11 kW/m² for a laminar flow, and 26.83 kW/m² for a turbulent flow. Differences in the corresponding surface heat transfer coefficients account for this variation: it was 5 W/(m²·K) for still air, 127 W/(m²·K) for laminar flow, and 218 W/(m²·K) for turbulent flow. We applied a 4 mm thick cork board insulator material to the interior unexposed airfoil laminate surface. Proceeding with a calculation method similar to the one in Appendix A, the required heat flux would now be 0.92 kW/m² in still air, 15.91 kW/m² for a laminar flow, and 26.63 kW/m² for a turbulent flow. These results were only slightly lower, because the heat transfer coefficient on the interior surface was already low (5 W/(m²·K)).

Subsequently, we opted to use polyimide electrothermal heating films with a heating capacity rating of 15.50 kW/m² at 115 volts (model KHA-112/10, OMEGA Engineering, Norwalk, USA). We considered this capacity sufficient for our laboratory experiments. This film type consists of a thin etched metallic foil resistive heating element encapsulated between two insulating layers of polyimide. It is attractive for the IPS application because of its high surface aspect ratio, light weight, high contour flexibility, and good chemical and thermal resistance [48]. These films have been employed in electric vehicle interior heating, aircraft electronics temperature regulation, battery warming, and consumer appliances [49]. Although it is a mature technology, it can be further tested for aircraft anti-icing applications under glaze ice conditions, and it also serves here as a realistic basis for multiphysics icing simulations of the CFRP-based IPS. We considered that while coated electrothermal IPS are promising, most are currently in the developmental stage or their durability is somewhat unproven [50–53], and they also require additional provisions to implement with contact resistance-free bus connections [24].

2.3 Fabrication of IPS laminates

Polymer composite laminate flat panels with integrated heating films were fabricated to characterize and validate their properties, and also to evaluate design parameters. The various parameters were the laminate stacking sequence, the presence of an aluminum foil shield and cork insulation, and the position and number of heating films. The overall panel area dimensions were 330 mm by 330 mm, with an 8-ply CFRP stack giving a nominal laminate thickness of 0.96 mm. The heating films each measured 25 mm wide, 305 mm

long, and 0.114 mm thick, and weighed around 3.43 g excluding their 305 mm long lead wires, giving an aerial weight of 450 g/m². The films were directly co-cured with the CFRP, either inserted in the place of a cut-out CFRP ply equivalent area section, or installed on top of the ply stack. We note that the adhesion between the polyimide and epoxy can be further improved, for example by plasma surface treatment [54].

The ply stack was sealed in a vacuum bag and cured in an autoclave oven up to 120°C at 6 atm pressure. The heating films were always aligned in the reference 0° laminate direction, which here coincides with the wingspan direction (x-axis). We selected an orthotropic laminate stacking sequence that favors the wingspan direction, which is coherent for aircraft wing skin [55]. If the laminate equivalent thermal conductivity coefficient is greater perpendicular to the heating film axis (k_{y_eq}), it should provide a more beneficial even surface temperature distribution, based on the Fourier's law of heat conduction. Accordingly, we evaluated the k_{y_eq} of a selected group of stacking sequences with a quasi-equivalent Young's modulus in the x-axis direction: laminates $[0_2/45/-45]_S$, $[90/0/27/-27]_S$, and $[90/36/0_2]_S$. The k_{y_eq} coefficient was calculated following a procedure outlined by Kulkarni and Brady [56]. It was found that $[90/0/27/-27]_S$ had the highest value ($k_{y\_eq} = 5.67$ W/(m·°C)), versus $[90/36/0_2]_S$ ($k_{y\_eq} = 4.84$ W/(m·°C)), and $[0_2/45/-45]_S$ ($k_{y\_eq} = 4.52$ W/(m·°C)). A higher calculated k_{y_eq} value essentially comes from a higher average y-axis direction component of the ply conductivity coefficient, which is defined as $k_y = |k_1 \cdot \sin(\theta)| + |k_2 \cdot \cos(\theta)|$, where k_1 and k_2 are the usual in-plane ply directional conductivity coefficients, and θ is the ply orientation angle. We note that the equivalent Young's modulus is governed by classical laminate theory, which otherwise involves the ply's elastic properties. The higher k_{y_eq} $[90/0/27/-27]_S$ stacking sequence was thus favored to fabricate the test panels.

Five different laminate panels were fabricated, as detailed in Table 3 and shown in Figs. 2–3. The heating films in Panels 1–4 were inserted in the second ply next to the outside surface. This was intended to position the heating films near the surface to be heated without exposing them to the elements. For Panels 2–4, a 0.1 mm thick aluminum foil was cleaned with acetone and co-cured on top of the last laminate ply. This was to test with the thermal benefit of a representative high conducting metallic erosion shield. Panels 3–4 also had a 4.6 mm thick cork board co-cured under the ply stack, to test the thermal effect of an insulating material applied on the inside surface. We observed, however, that the cure cycle caused the corkboard to permanently collapse to a thickness of 1.7 mm. The CFRP and heating films in Panel 5 were first co-cured together, with the films on top of the ply stack to keep the CFRP laminate integral, and to verify the thermal properties of this configuration. A corkboard and aluminum foil were then adhered under vacuum pressure only using room temperature cure epoxy adhesive paste with a bond line thickness of 0.17 mm (Loctite EA 9394 AERO, Henkel Corporation Aerospace, Bay Point, USA). This cure sequence preserved the corkboard's initial thickness and prevented residual wrapping from the un-symmetric laminate configuration. Panels 4 and 5 had two heating films separated by a gap of 75 mm and 50 mm, respectively, meant to represent a length of 2–2.5 heating film width. This choice was to experimentally verify how the gap distance affects the potential drop in surface temperature between the heating film units.

Table 3: Fabricated composite laminates with electrothermal films.

| Panel number	Heating capacity [kW/m²]	Stacking sequence	Description	Overall thickness [mm]
1	15.5	$[0_2/45/-45]_S$	CFRP only Heater in 2nd ply	0.96
2	15.5	$[90/0/27/-27]_S$	Aluminum/CFRP Heater in 2nd ply	1.06
3	15.5	$[90/0/27/-27]_S$	Aluminum/CFRP/Cork Heater in 2nd ply	2.76
4	2 × 15.5	$[90/0/27/-27]_S$	Aluminum/CFRP/Cork Heaters in 2nd ply, gap of 75 mm	2.76
5	2 × 15.5	$[90/0/27/-27]_S$	Aluminum/Epoxy/CFRP/Epoxy/Cork Heaters under 8th ply, gap of 50 mm	6.00
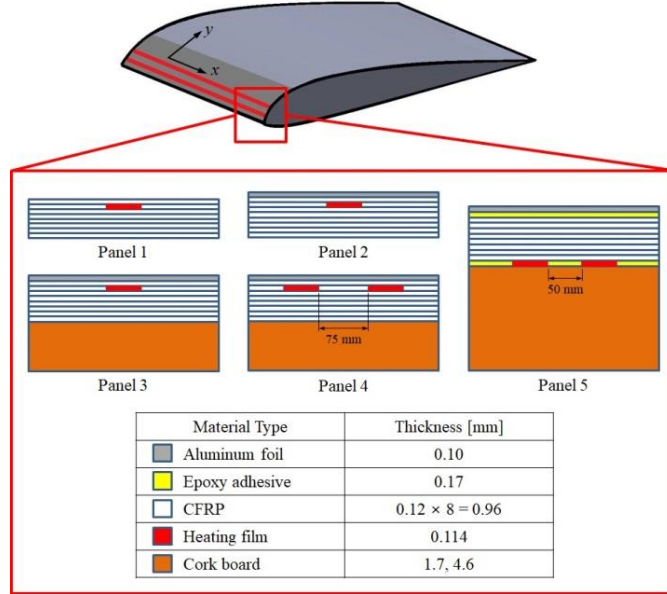
Figure 2: Schematic representation of the fabricated laminate panel cross-section configurations.
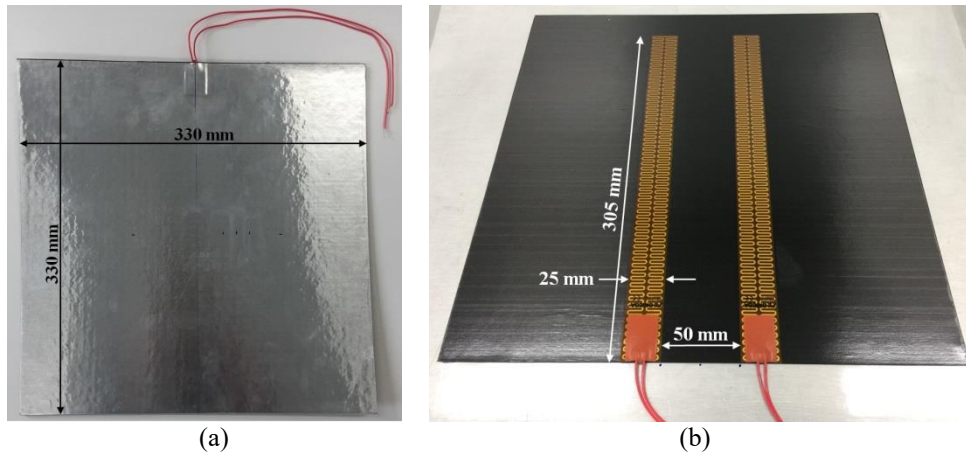

| (a) | (b) |

Figure 3: CFRP-based IPS laminate panels: (a) Panel 2, (b) Panel 5 before adhesion of corkboard and aluminum foil.

2.4 Thermal response of the IPS laminates

The thermal response of the IPS panels was tested by applying an electrical voltage to the heating films from a direct current (DC) power supply (model DRP-9303, Digital Electronics Co. Ltd., Incheon, South Korea), with the panel resting horizontally at an ambient room temperature of 26±1°C (Fig. 4). The panel upper surface temperature was measured with four Type-K thermocouples affixed with high-temperature adhesive tape. The thermocouples were aligned as follows: one was aligned with the heating film's longitudinal centerline axis, and placed 25 mm, 37.5 mm, and 50 mm away laterally for Panels 1−4, and placed 22.5 mm, 30 mm, and 37.5 mm away laterally for Panel 5. A four-channel thermocouple reader (model 176, Testo AG, Lenzkirch, Germany) recorded the temperatures to a computer at a rate of 1 Hz. The circuit resistance of each heating film was measured with an ohmmeter. Fig. 5 shows the temperature response over the heating film centerline axis for all panels tested. The temperature displays a characteristic logarithmic growth variation with time. If this transient thermal process is simplified as a lumped capacitance analytical model, it can then be represented as a first-order differential energy balance equation [39]. The solution to this equation has the form of the reciprocal of an exponential growth function as,

$$\frac{T(t)-T_0}{T_m-T_0} = 1 - e^{\frac{-t}{\tau_g}} \tag{1}$$

where T_0 and T_m are the initial and maximum steady-state temperatures respectively, and τ_g is a characteristic thermal growth time constant which is proportional to the time needed for temperature growth. The results in Fig. 5 were each individually fitted to the function of equation (1) by the least-squares method; this allows the test results to be presented more formally, as listed in Table 4.
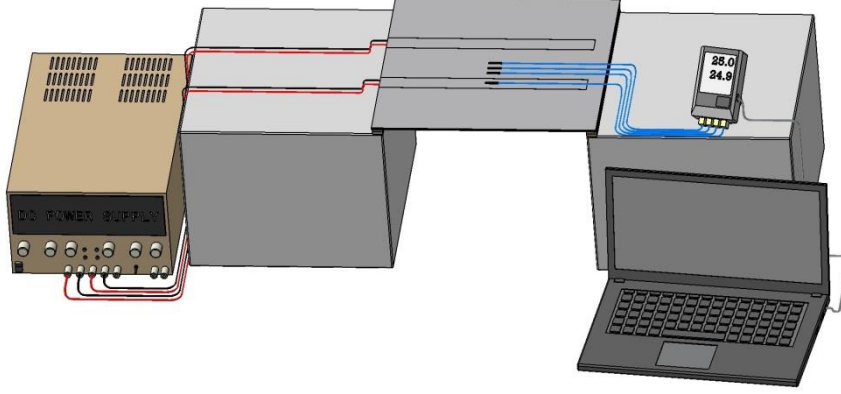

Figure 4: IPS laminate panel thermal response test setup.
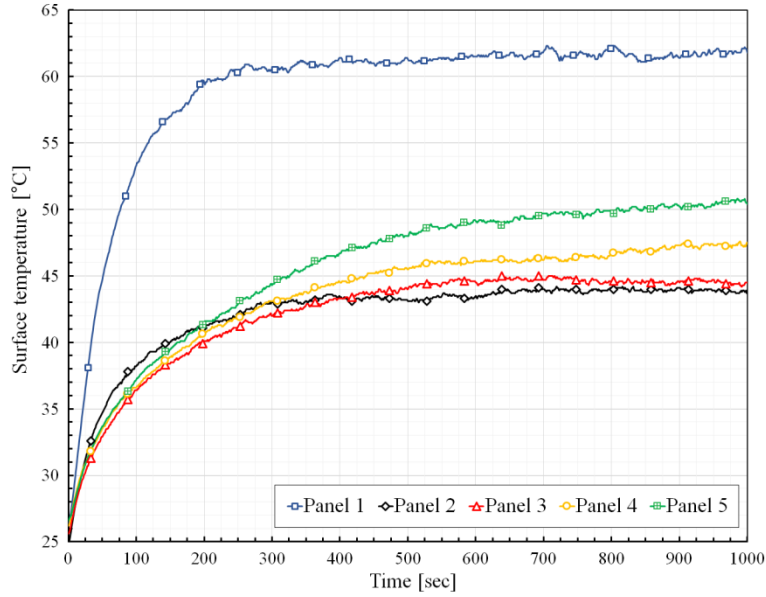
Figure 5: Test results showing the temperature at the heating film's centerline axis location.

Table 4: Thermal response test results.

Panel number	1	2	3	4	5
$(T_m - T_0)$ [°C]	34.7	18.9	19.1	21.2	24.7
τ_g [sec]	71.2	81.7	134.4	177.4	226.8
Applied voltage [V]	29.7	29.6	29.6	2 × 29.4	2 × 29.4
Heater circuit resistance [Ω]	111.0	110.4	110.0	109.8/110.2	109.8/110.1
Film heat flux [kW/m²]	1.04	1.04	1.04	1.03/1.03	1.03/1.03

The τ_g time constants were in the range of 71–227 sec, which follows from the test conditions used, in particular, the different panel laminate configurations and the relatively low applied heat flux level of around 1 kW/m². A fair comparison to other published results would thus be limited to those with similar conditions or at least laminates of similar strength.

In general, the temperature rise rate should be inversely proportional to the material's specific heat capacity (C_p) and the mass of the material to be heated up. This was confirmed by the τ_g test results, when adding the aluminum foil (81.7 sec. for Panel 2, versus 71.2 sec. for Panel 1), the cork insulation (134.4 sec. for Panel 3, versus 81.7 sec. for Panel 2), and the epoxy adhesive paste (226.8 sec. for Panel 5, versus 177.4 sec. for Panel 4). The heating films only covered a portion of the panel's surface; therefore, the panel's thermal conduction is expected to influence temperature distribution. Between Panels 1 and 2, which had a similar heat flux input, the aluminum foil of Panel 2 provided greater thermal conduction and caused a lower temperature rise over the heating film axis (18.9°C for Panel 2, versus 34.7°C for Panel 1). The lower temperature peaks provide a greater margin below the material's maximum operating temperature, and thus higher overall heating power inputs are possible.

3. Multiphysics anti-icing simulation of a CFRP composite structure

3.1 Thermal FEM of IPS laminates

Steady-state thermal finite element modeling (FEM) was performed for all the test panels, primarily to validate the material's thermal properties. The panels were modeled with 8-node linear heat transfer brick solid elements using the software Abaqus/CAE 6.14-2 (Dassault Systèmes SE, Vélizy-Villacoublay, France). There was one element per CFRP ply in the thickness direction, and a nominal in-plane mesh size of 2.5 mm × 2.5 mm (Fig. 6). The material thermal conductivity was modeled either as orthotropic (CFRP composite) or isotropic (aluminum, cork, heating film). The ply angles in the CFRP laminate were implemented by orienting the section property of each ply layer element to their corresponding angle. The heating film was modeled as a heater core layer sandwiched by polyimide layers. The heater core layer, which contained the metallic foil element, had a thermal conductivity coefficient between polyimide and a metallic wire material ($k = 35$ W/(m·°C)). A surface film heat transfer coefficient (h) was applied to all exterior surfaces, with a sink temperature of 26°C. The heating film heat source was modeled with a body heat flux load applied to the film core. The magnitude of the heat flux (P) was determined according to the Joule–Lenz law and assuming an ideal Ohm resistor,

$$P = \left.\left(\frac{V^2}{R}\right)\middle/ V_{heater}\right. \quad \left[\frac{\text{W}}{\text{m}^3}\right], \tag{2}$$

where V is the applied circuit voltage in the test, R is the heating film circuit resistance, and V_{heater} is the volume of the film core modeled in FEM.

$$\overline{Nu}_{L\_upper} = 0.54 \cdot Ra_L^{1/4} \quad (10^4 \leq \text{Ra}_L \geq 10^7) \tag{3}$$

$$\overline{Nu}_{L\_lower} = 0.27 \cdot Ra_L^{1/4} \quad (10^5 \leq \text{Ra}_L \geq 10^{10}) \tag{4}$$

$$Ra_L = \frac{g\beta(T_s - T_\infty)L^3}{\nu\alpha} \quad \{T \sim °K\} \tag{5}$$

$$\overline{Nu}_L = \frac{\overline{h_{conv}} \cdot L}{k} \tag{6}$$

$$\overline{h_{rad}} = \varepsilon\sigma(T_s + T_\infty)(T_s^2 + T_\infty^2) \quad \{T \sim °K\} \tag{7}$$

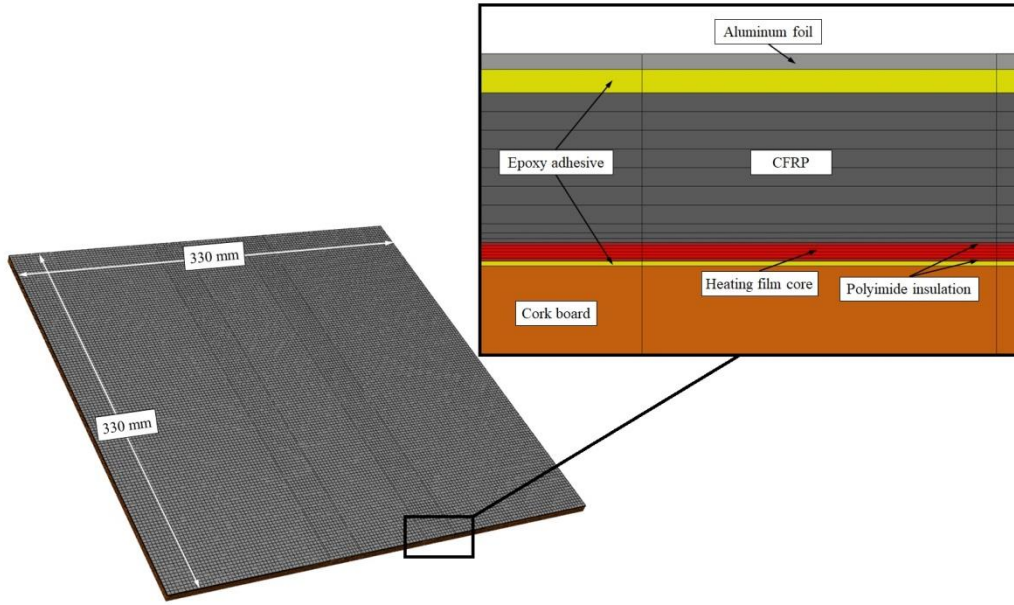$$T_{\bar{s}} = T_\infty + \omega_d(T_m - T_\infty) \quad \{T \sim °K\} \tag{8}$$

Figure 6: Finite element model of Panel 5.

We used empirical correlations to determine the convection heat transfer coefficients in still air [39]. The average Nusselt number (Nu) of both the upper and lower surfaces was first calculated using equations (3)-(4), where Ra_L is the characteristic Rayleigh number. The Rayleigh number is defined in equation (5), where g is the gravity constant, β is the air thermal expansion coefficient, T_s is the panel surface temperature, T_∞ is the ambient temperature, L is the panel's characteristic length, v is the air kinematic viscosity, and α is the air thermal diffusivity. Here L was taken to be the panel surface area divided by its perimeter length. An average convection heat transfer coefficient ($\overline{h_{conv}}$) was then calculated from the usual Nu definition in equation (6), where k is the air thermal conductivity. The average radiation heat transfer coefficients from the plate to the surroundings were calculated with equation (7), where ε is the panel surface emissivity and σ is the Stefan-Boltzmann constant ($\sigma = 5.67 \times 10^{-8}$ W/m^2·K^4). The applied h values were the sum of the convection and radiation components for each respective panel surface (upper/lower), and an average of these for the panel sides. Since the surface temperature is not uniform over the panel area, we chose to use the average surface temperature value ($T_{\bar{s}}$) in the length over the heating film width (w_{hf}) and one width on each side ($3w_{hf} = 75$ mm) for the convection heat transfer coefficient calculations. The rationale for this choice is to consider that the majority of the heat transfer occurs in this area. This $T_{\bar{s}}$ value was set by iterating the FEM results, and it is expressed here in the form of equation (8), where ω_d represents a temperature distribution form factor. The air properties were taken at the film temperature (T_f), which is defined as the average of the ambient and average surface temperatures ($T_f = avg\{T_\infty, T_{\bar{s}}\}$). The calculated heat transfer coefficients are listed in Table 5.

Table 5: Surface heat transfer coefficient calculations.

Panel number	1	2	3	4	5
$T_{\bar{s}}$ [°K]	316.5	312.9	313.5	315.9	319.7
ω_d	0.50	0.73	0.75	0.79	0.83
Ra_L	7.50E+5	6.42E+5	6.65E+5	7.63E+5	9.08E+5
$h_{avg\_conv\_upper}$ [W/m^2·°C]	5.26	4.96	5.00	5.20	5.45
$h_{avg\_conv\_lower}$ [W/m^2·°C]	2.63	2.48	2.50	2.60	2.73
$h_{avg\_rad\_upper}$ [W/m^2·°C]	4.63	1.63	1.63	1.65	1.68
$h_{avg\_rad\_lower}$ [W/m^2·°C]	4.63	4.55	6.07	6.14	6.25

3.2 IPS laminate thermal FEM results

Figure 7 shows an example of the FEM simulation temperature distribution results with the double heating film Panel 5. The agreement between the FEM and test results for each panel was evaluated by a Euclidean norm of the temperature differences at the thermocouple locations,

$$l_2\text{-}norm = \sqrt{\sum_{i=1}^{4}(T_{FEM} - T_{test})_i^2} \qquad (9)$$

The individual temperature differences are listed in Table 6, where the location of T_1 corresponds to the heating film centerline axis, and the others follow in the order of distance from the axis. The majority of temperatures are in agreement within 1°C, with an extremum deviation range of -0.63 to 1.54°C. The deviations may be caused by using constant thermal conductivity coefficients and uniform surface heat transfer coefficients in the FEM, and also by thermocouple position and measurement deviations.
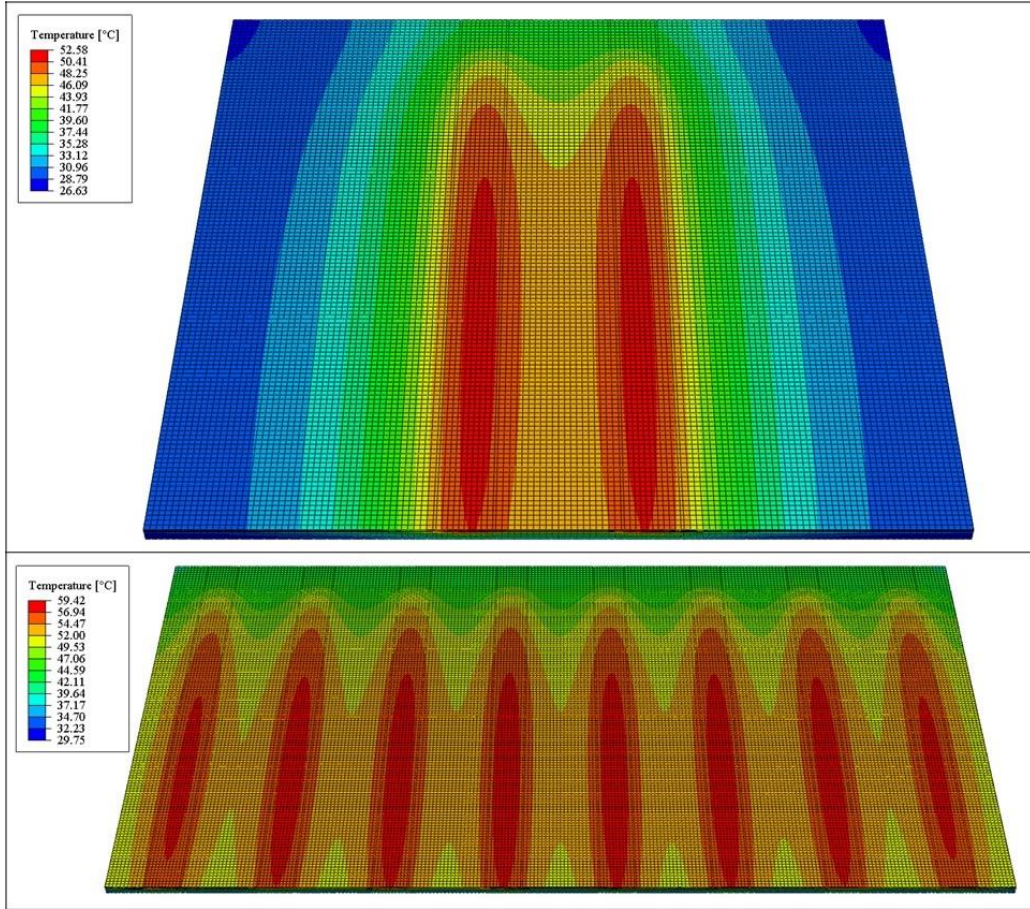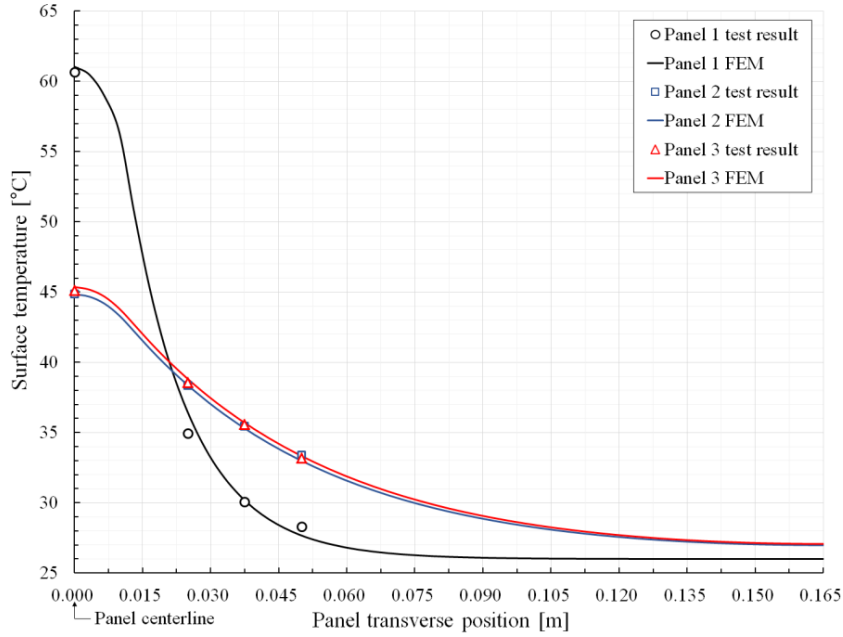

Figure 7: FEM steady-state temperature distribution of Panel 5 (top) and Panel 5 – 8 heaters (bottom).

Table 6: Temperature difference between FEM and test results.

	ΔT_1 [°C]	ΔT_2 [°C]	ΔT_3 [°C]	ΔT_4 [°C]	l_2-norm [°C]
Panel 1	0.37	1.54	0.14	-0.63	1.71
Panel 2	0.00	0.02	-0.14	-0.41	0.44
Panel 3	0.25	0.27	0.13	0.16	0.43
Panel 4	-0.02	1.17	1.46	1.30	2.28
Panel 5	0.29	0.90	0.45	0.43	1.13

Figure 8 presents a graphical comparison of the steady-state surface temperature distribution for the FEM and test results. One-half of the temperature distribution is presented owing to the panels' transverse symmetry. It is noticeable in Fig. 8(a) that the more conductive aluminum foil on Panels 2 and 3 favors greater lateral thermal conduction compared to Panel 1. Indeed, for example, the calculated equivalent lateral thermal conductivity coefficient (k_{y_eq}) of Panel 2 is 25.70 W/(m·°C) when the aluminum foil is included, compared to 5.67 W/(m·°C) when it is not. We also observed comparatively that the addition of corkboard insulation in Panel 3, compressed to a 1.7 mm thickness, only caused a minor beneficial increase in the surface temperature. In the double heating film results of Fig. 8(b), the temperature drop between heating films was around 8.5°C for Panel 4 and around 4.4°C for Panel 5.
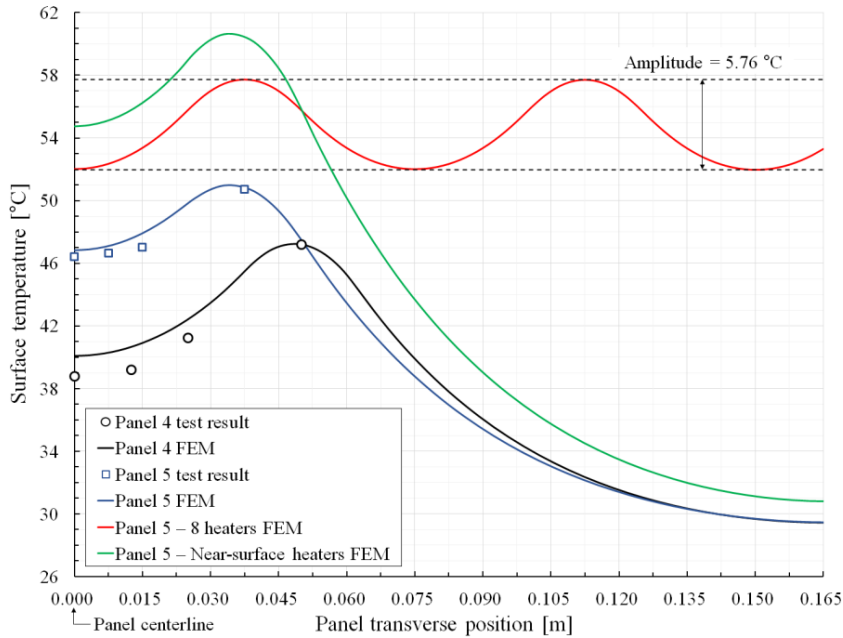
Figure 8: Steady-state temperature distribution for FEM and test results: (a) single heating film panels; (b) double heating film panels.

The configuration in Panel 5 was used to model a condition of continuous heating film distribution. This model consisted of a panel with an extended width of 600 mm, and 8 heating films separated by 50 mm gaps. With the same power input and heat transfer conditions, the simulated temperature drop between heating films was 5.76°C (Fig. 8(b)). We also noted there was a higher maximum surface temperature, caused by the cumulative heat flux from all the adjacent heating films.

In another design study with the Panel 5 FEM model, the position of the heating films was moved up within the epoxy adhesive layer between the aluminum foil and the CFRP laminate. Again with the same power input and heat transfer conditions, the simulated maximum surface temperature was 9.65°C higher than the original Panel 5 configuration (60.62°C vs 50.97°C), although the maximum temperature drop between heating films was still around 6°C. This near-surface heater configuration would still have a net thermal advantage. In this case, the CFRP essentially acts as a thermal barrier, since its through-thickness thermal conductivity coefficient is much lower compared to the aluminum foil (0.95 W/(m·°C) versus 218 W/(m·°C)). This configuration may require attention, to keep the adhesive bond line between the heating films and the aluminum foil thin enough to keep weight low, while avoiding the heating films imprinting on the thin aluminum foil.

3.3 Multiphysics anti-icing simulation in glaze ice conditions

The preceding thermal FEM simulation can be readily extended to solid/fluid modeling of a dry airflow over an IPS airfoil. A further step is to consider icing conditions in the dynamic airflow, to represent "wet" airflow multiphysics icing simulation. This method presents the atmospheric icing conditions that may be encountered by an aircraft. Evaluating an IPS experimentally would involve high cost, scaling issues, and long run times, and that would make it infeasible to simulate all of the metrological conditions prescribed by icing certification envelopes. Alternatively, multiphysics simulation has a much lower cost compared to using an icing wind tunnel, and it can more easily cover all metrological conditions. It is worth mentioning that this simulation method has been used extensively in the aircraft icing certification process [7].

Hence in this study, the simulation of ice accretion and anti-icing on an airfoil was performed using the extensively-validated commercial software ANSYS FENSAP-ICE (ANSYS Inc., Canonsburg, USA) [8]. This high-fidelity software is based on partial differential equation formulations and can concurrently solve the dynamic airflow over the airfoil, the formation of ice for given icing conditions, and the heat transfer from an IPS.

An overview of the multiphysics icing simulation procedure is shown in Fig. 9. The viscous airflow field around the clean airfoil shape is first determined with a classic compressible Navier-Stokes-Fourier formulation and a Spalart-Allmaras turbulence model. This solution is then used in a one-way coupling calculation to determine the water droplet flow. The water droplet impingement collection efficiency is then predicted using a distinct solver (DROP3D) [57]. The collection efficiency is defined as the normalized influx of water at a given location; it can thus quantitatively measure the potential of droplets to collect and subsequently generate ice-accretion [58]. The ice shape on the surface is predicted using a thermodynamic solver (ICE3D) with the air frictional shear stress and heat flux on the solid surface obtained from the flow field velocity and temperature solution, and the droplet impact velocity and collection efficiency on the solid surface obtained from the DROP3D module. Finally, a conjugate heat transfer module (CHT3D) based on coupled heat convection and conduction equations (module C3D) is used along with all the other modules to complete the simulation [59]. Heat conduction in the airfoil skin and heat generation from the IPS is implemented in a finite element formulation through the law of conservation of energy,

$$\frac{\partial H_M(T)}{\partial t} = \nabla \cdot (k_M(T)\nabla T) + S_M(t),$$
(10)

where for every material M, H_M is the material enthalpy, k_M is the material thermal conductivity coefficient, S_M is the volumetric heat source (here from heating films), T is the material temperature, and t is the simulation time. All of the different simulation modules are executed successively and coupled sequentially in FENSAP-ICE within every time step for a chosen simulation time, and this allows

the visualization of ice formation and melting. From the software user standpoint, the overall simulation procedure is a one-step process, and it can capture the transient formation and melting of ice in order to predict the efficiency of an IPS.
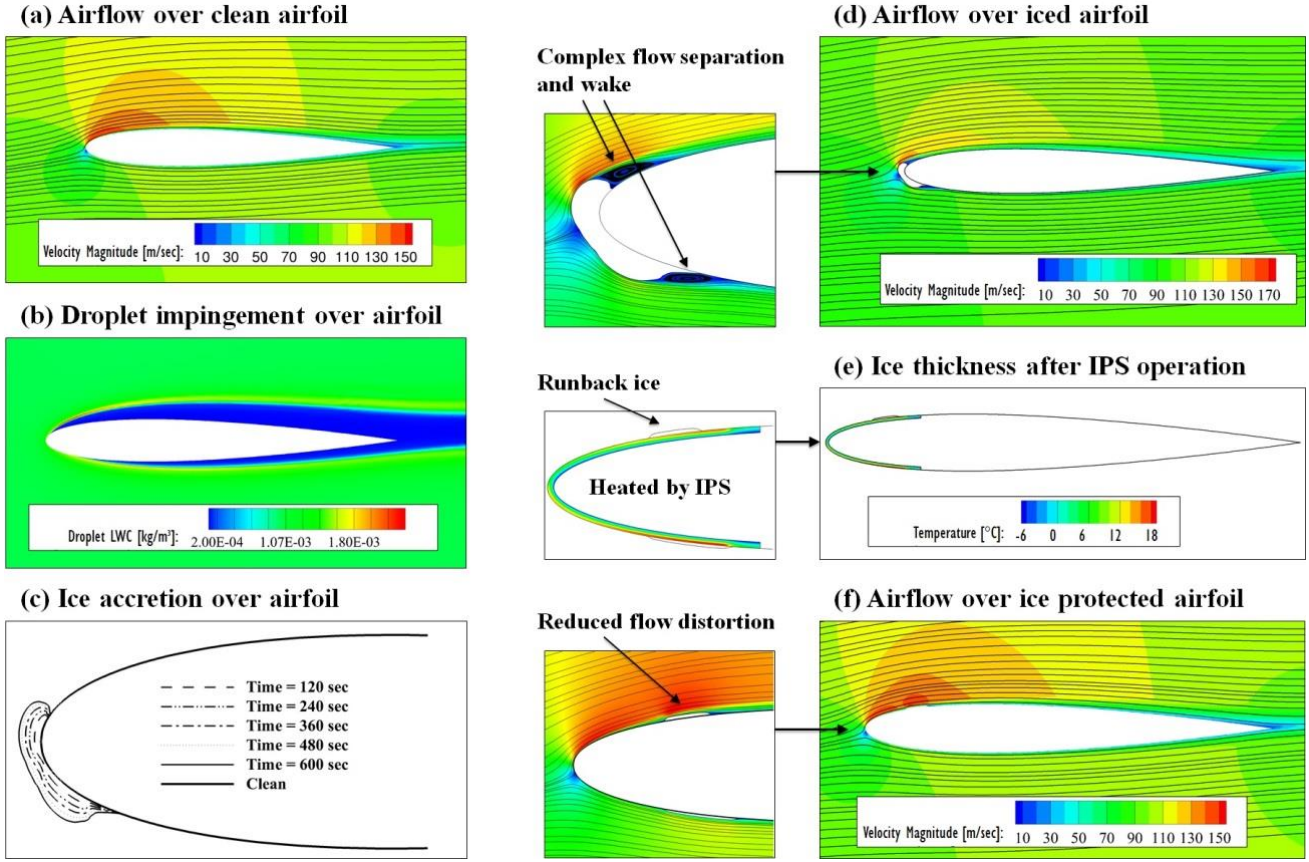

Figure 9: Overview of the multiphysics icing simulation procedure.

The model of a CFRP NACA0012 airfoil with an IPS based on the original laminate configuration of Panel 5 was constructed in the ANSYS FENSAP-ICE software. This model is two-dimensional, but we expect that for the present UAV aircraft type, the simulation results will be consistent with the actual physics, since the wing is straight with no swept angle and no taper, and the wing aspect ratio (span/chord) is moderate to large. The panel 5 laminate configuration was selected because in practice it would keep the CFRP laminate integral. The performance of this IPS was investigated in icing conditions selected from the FAR Part 25 Appendix C standard [29]. We considered two IPS designs: i) 5 heating films with spacing gaps of 50 mm, and ii) 15 heating films with spacing gaps of 2 mm. Each heating film covered a distance of 25 mm (i.e., the film width), and they were positioned symmetrically around the leading edge with uniform spacing gaps between them. The airfoil had a chord length of 1 m, which is a realistic value for this type of UAV aircraft. The stacking sequence of Panel 5, as described in Fig. 2 and Table 3, was implemented in the model along with the individual material properties. Presently the software is only applicable to isotropic thermal material models. Since the current airfoil simulation model has a two-dimensional nature, an equivalent isotropic CFRP thermal conductivity coefficient ($\bar{k}$) was determined as the arithmetic mean of the laminate equivalent thermal conductivity coefficients of Panel 5 in the x-axis direction (5.67 W/(m·°C)) and through-thickness direction (0.95 W/(m·°C)): $\bar{k}$ = 3.31 W/(m·°C). Fig. 10 shows the overall fluid/solid computation domain with grid definition and boundary conditions, and a close-up view of the solid IPS airfoil model having 15 heating film units. The solid surfaces had non-slip boundary conditions, and far-field Riemann invariant conditions were applied to the outer boundaries of the fluid domain.
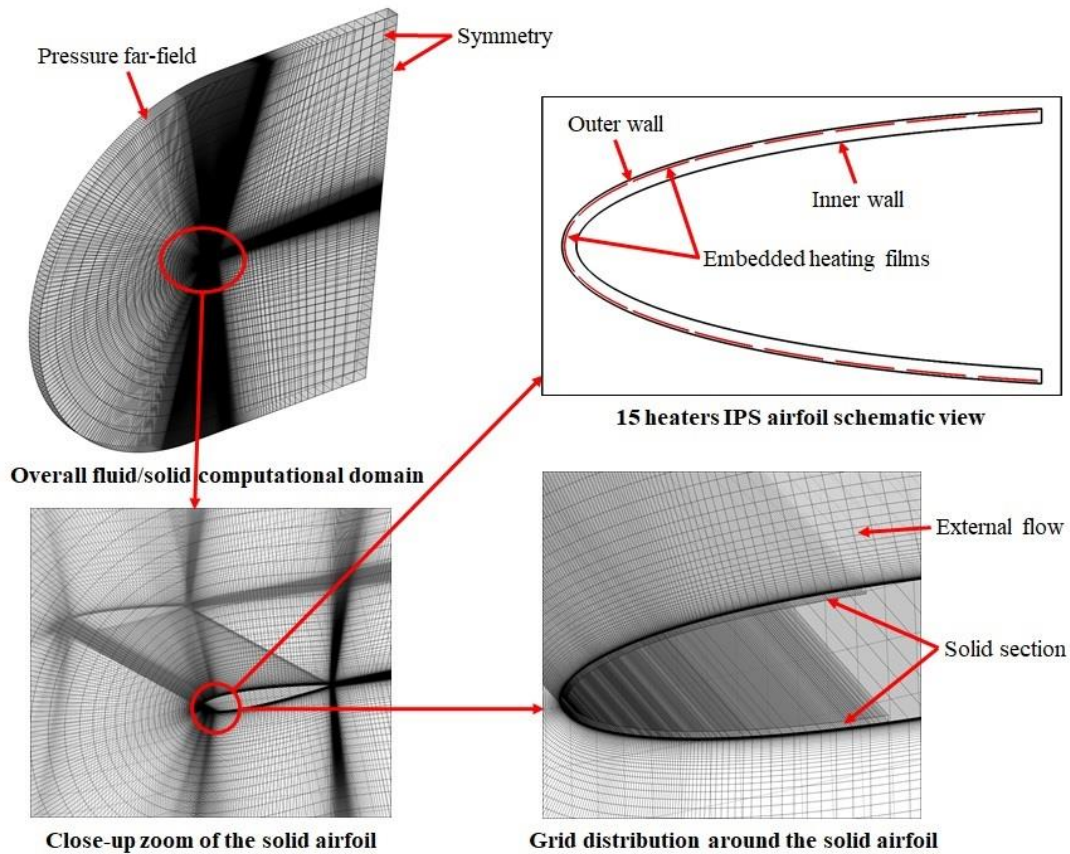
Figure 10: Computational domain of the multiphysics icing simulation model.

The icing flight conditions used in the simulations were an airflow velocity of 102 m/sec (367.2 km/h), air temperature of -6.65°C, water droplet median volume diameter (MVD) of 20 μm, cloud liquid water content (LWC) of 0.78 g/m^3, and an exposure time of 600 sec, which together represent a possible icing exposure scenario. We considered two distinct airfoil angle of attack (AOA) values of 0° and 4°, and IPS heat flux values of 0, 2.5, 5, 7.5, or 10 kW/m^2. Any selected heat flux level was applied equally to all heating films for a given IPS.

3.4 Multiphysics anti-icing simulation results

Figures 11–12 show the ice accretion prediction results around the NACA0012 airfoil for the two IPS designs after 600 sec of simulation and at varying IPS heat fluxes and airfoil AOA. In the case of the 5 heater IPS (Fig. 11), the ice accretion was only partially removed even when the heat flux was increased up to 10 kW/m^2. This is in part due to the runback of melted ice and the spacing gap distance between heating films. Melted ice water that travels aft on the airfoil surface and then encounters a cooler surface temperature in the heating film gap zone may re-freeze, creating what is called *runback ice*. This phenomenon was observed at both 0° and 4° AOA.
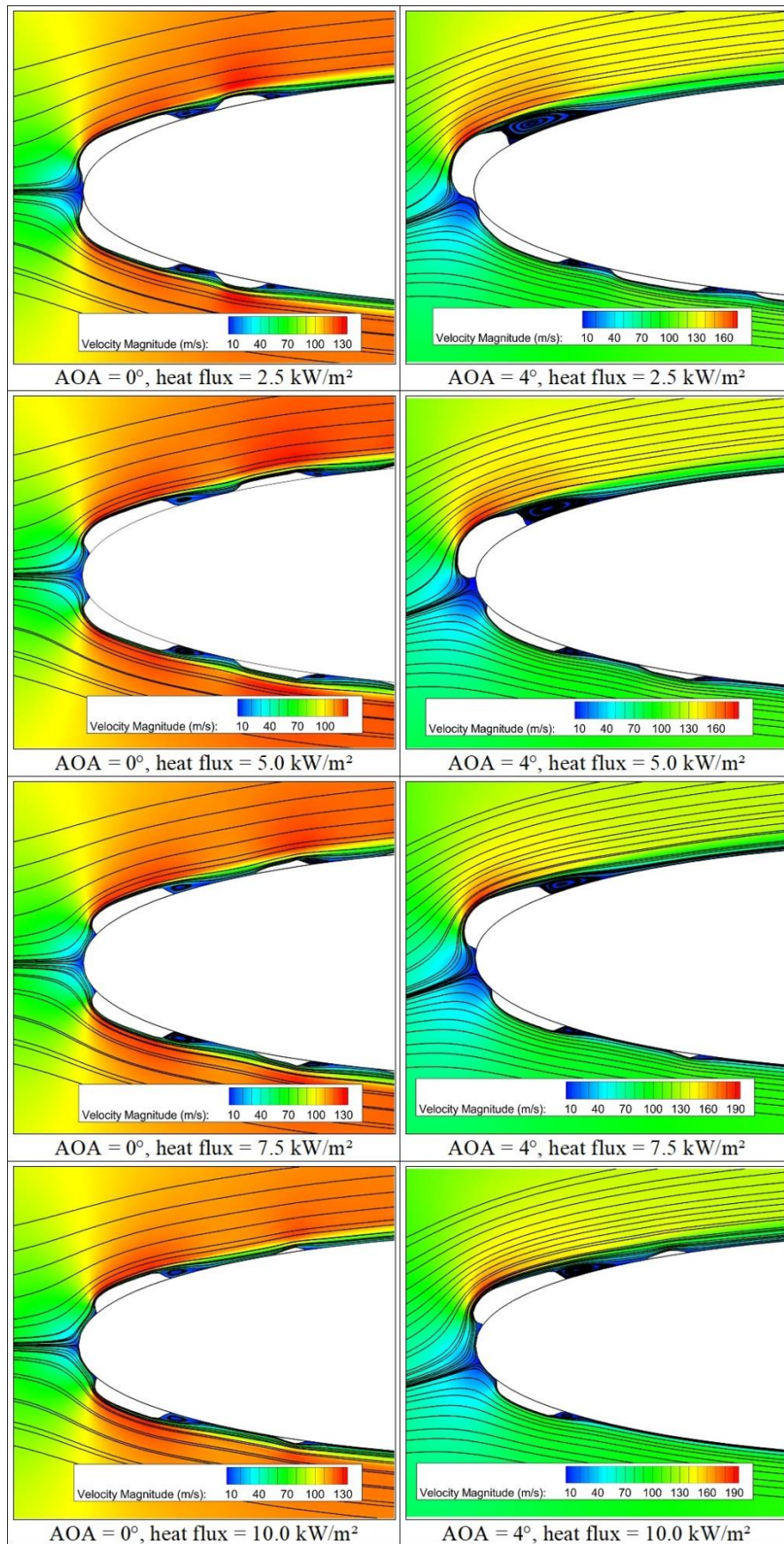
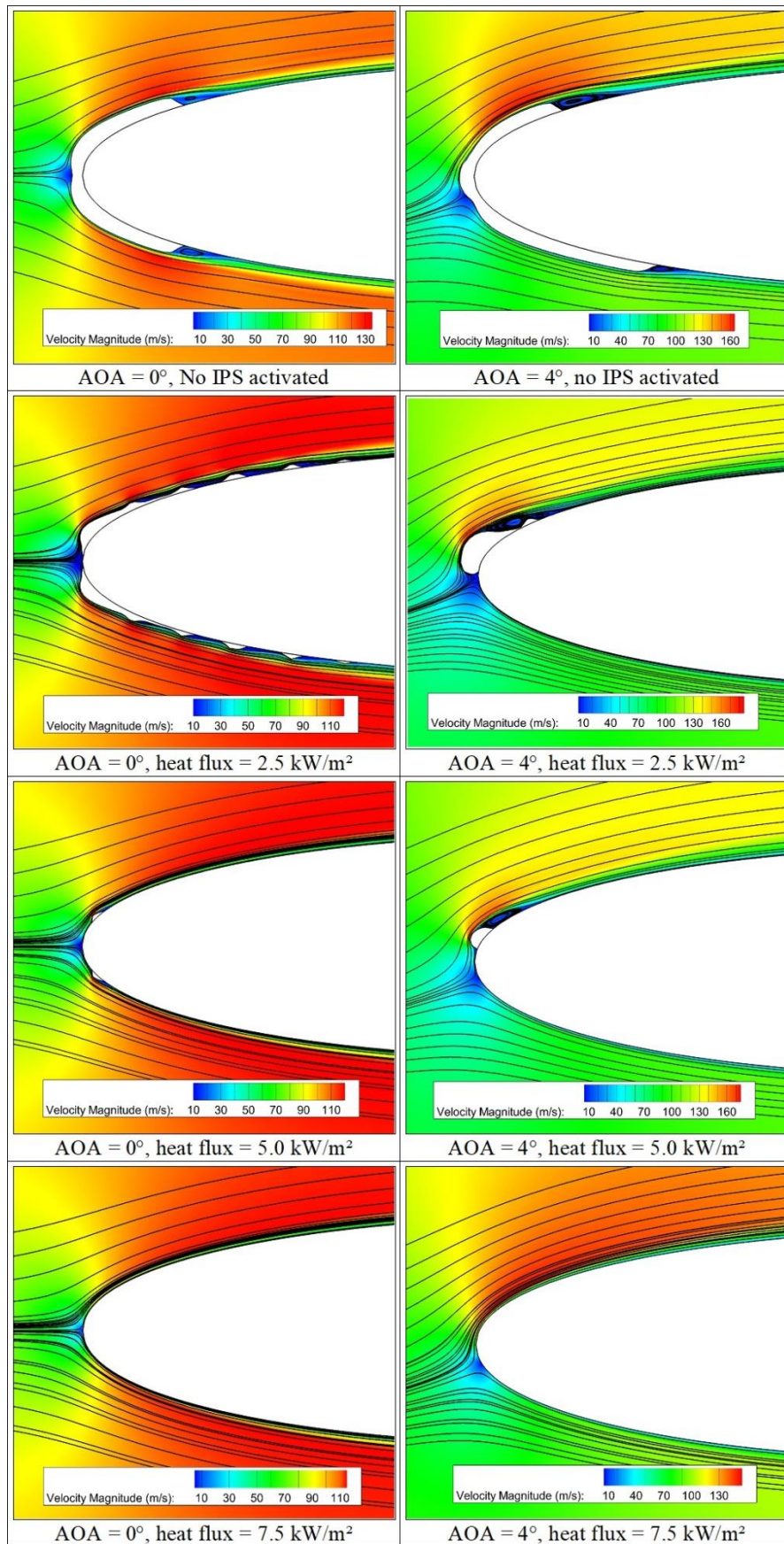Figure 11: Airflow streamlines and ice accretion simulation results for the 5-heater IPS airfoil.

Figure 12: Airflow streamlines and ice accretion simulation results for the 15-heater IPS airfoil.

With the 15 heater IPS (Fig. 12), it was clear that starting with a considerable amount of accreted ice when the IPS was not activated, ice was only partially removed with the 2.5 kW/m² or 5.0 kW/m² IPS heat fluxes, however there was no trace of ice with a 7.5 kW/m² IPS heat flux. We verified that the ice accretion on the upper and lower surfaces was always symmetric for both IPS designs at 0° AOA; in this case, gravity has a negligible effect. Conversely, the ice accretion location and thickness were more varied with a 4° AOA. In Fig. 12, runback ice was found for a 2.5 kW/m² IPS heat flux and 0° AOA, but it did not appear with 4° AOA. Instead, a frontal "ice horn" of considerable height was formed, which may be due to local flow acceleration on the upper surface. Flow acceleration generally increases convective cooling [60], which here may consequently be the cause of this clustered ice accretion on the upper airfoil surface.

Figures 13–14 shows images of the temperature distribution in the airfoil skin solid material and its outside surface for the two IPS designs at varying IPS heat fluxes and airfoil AOA. In Fig. 13(a) for the 5 heaters IPS, it is clear that the solid airfoil temperature fluctuates between zones of heating films and spacing gaps. Areas of ice accretion are adjacent to airfoil regions with a temperature below 0°C. Otherwise, for the 15 heaters IPS results in Fig. 14(a), the solid airfoil temperature distribution is more uniform. It is still noticeable that the lower part of the airfoil is cooler for the case of {2.5 kW/m², 4°}, and that for a heat flux of 7.5 kW/m², higher temperature zones near the airfoil outside surface exist at the location of the aft positioned heating film units. Those local higher temperature zones are in part indicative of the thermal insulation provided by the corkboard layer.
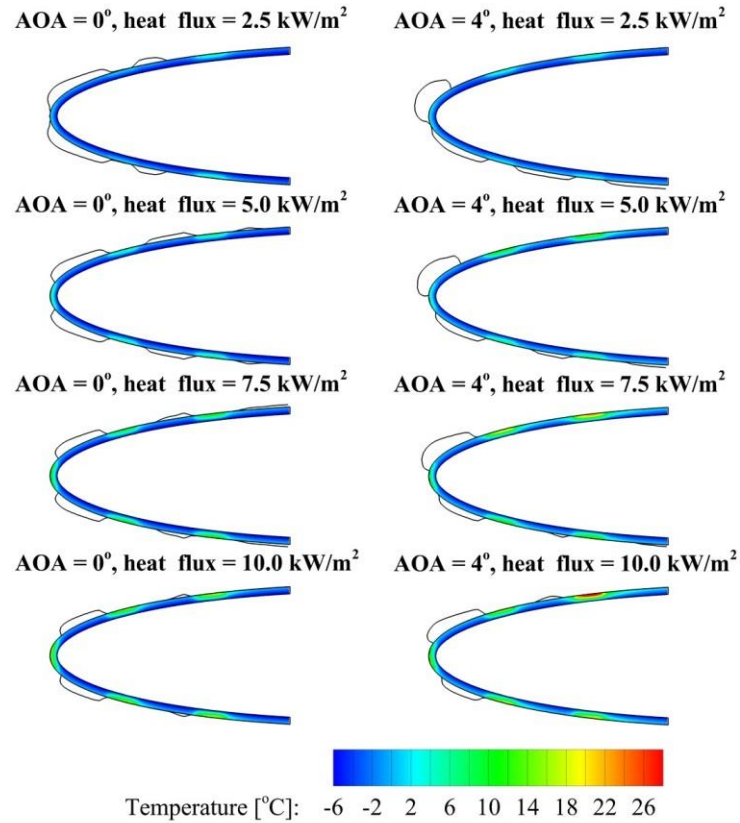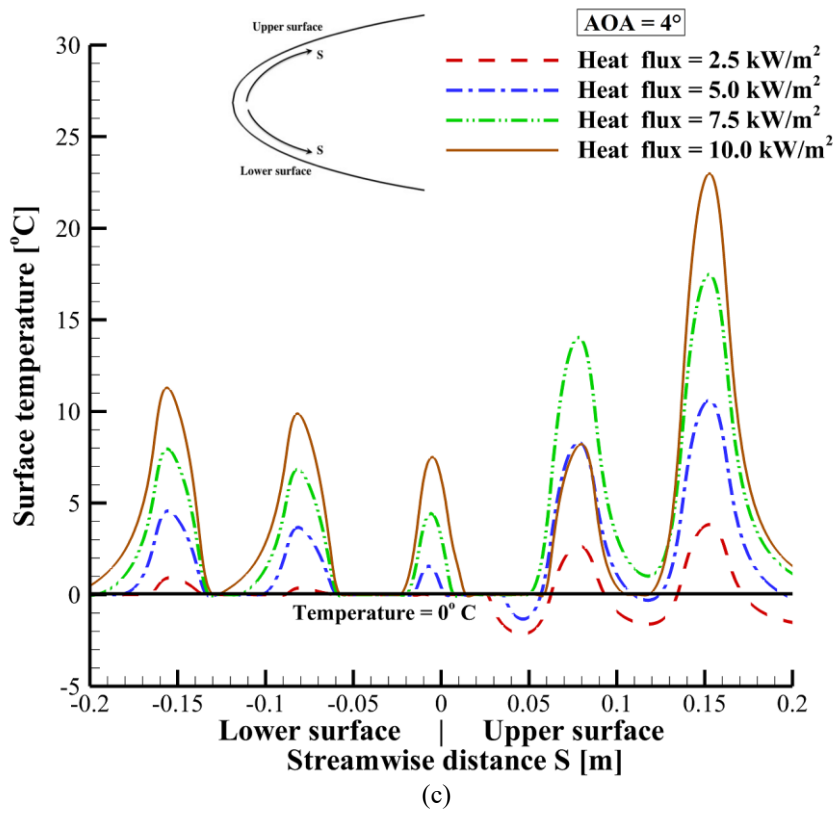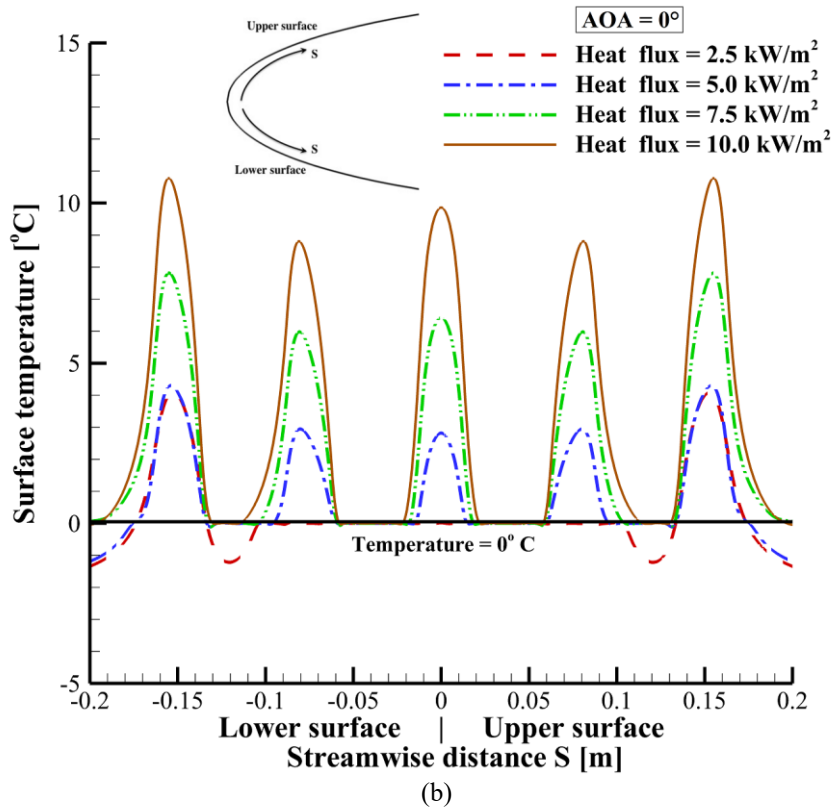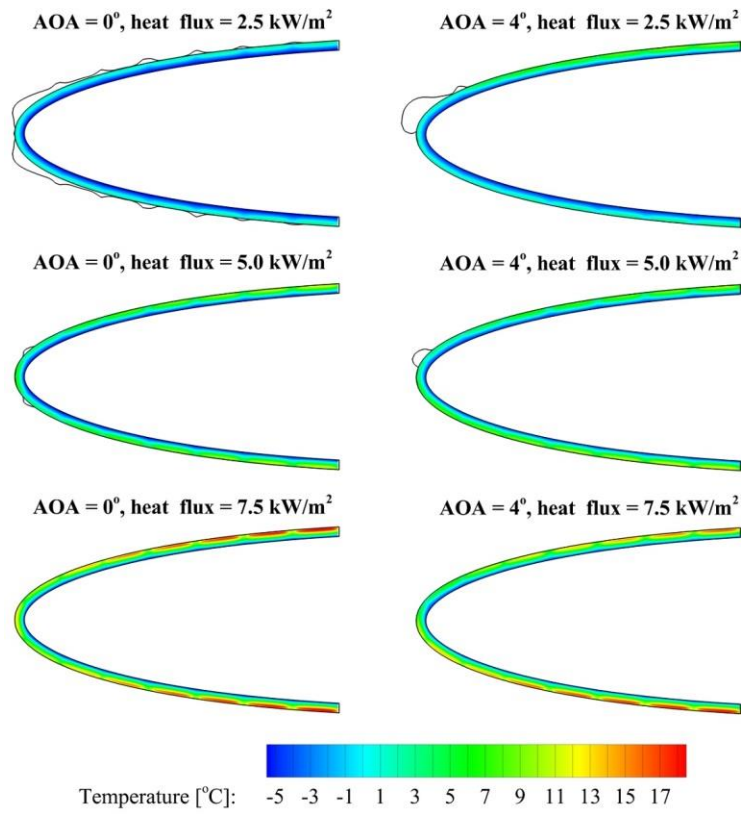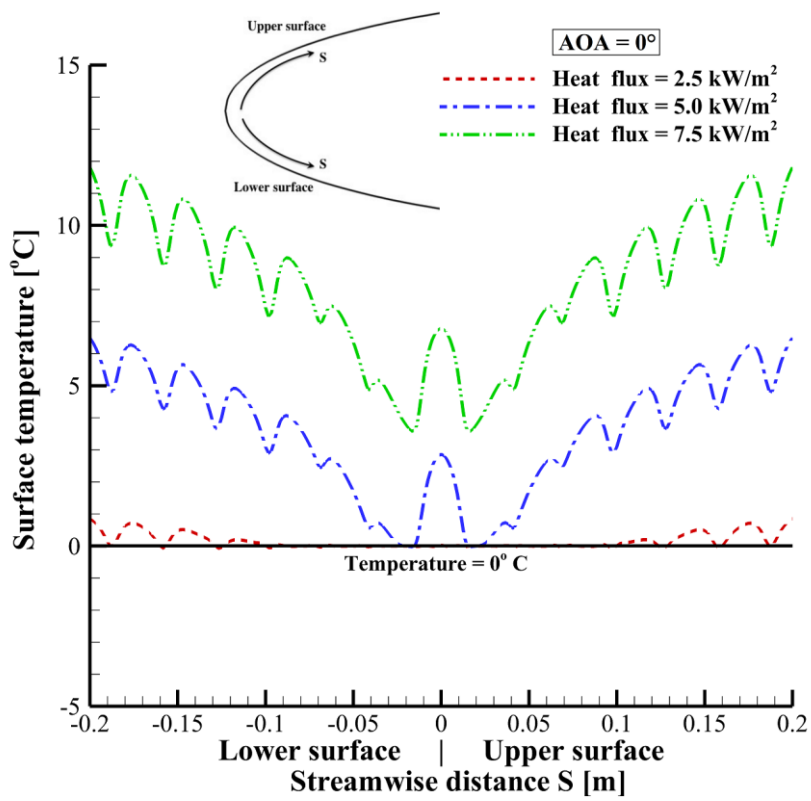

(a)

Figure 13: Multiphysics simulation results for the 5-heater IPS airfoil: (a) airfoil section temperature contours in the IPS region; (b) airfoil surface temperature for AOA = 0°; (c) airfoil surface temperature for AOA = 4°.

19

AOA = 0°, heat flux = 2.5 kW/m²   AOA = 4°, heat flux = 2.5 kW/m²

AOA = 0°, heat flux = 5.0 kW/m²   AOA = 4°, heat flux = 5.0 kW/m²

AOA = 0°, heat flux = 7.5 kW/m²   AOA = 4°, heat flux = 7.5 kW/m²

Temperature [°C]:   -5 -3 -1 1 3 5 7 9 11 13 15 17

(a)

(b)

Upper surface

S

Lower surface

S

AOA = 0°

Heat flux = 2.5 kW/m²
Heat flux = 5.0 kW/m²
Heat flux = 7.5 kW/m²

Temperature = 0° C

Lower surface | Upper surface

Surface temperature [°C]
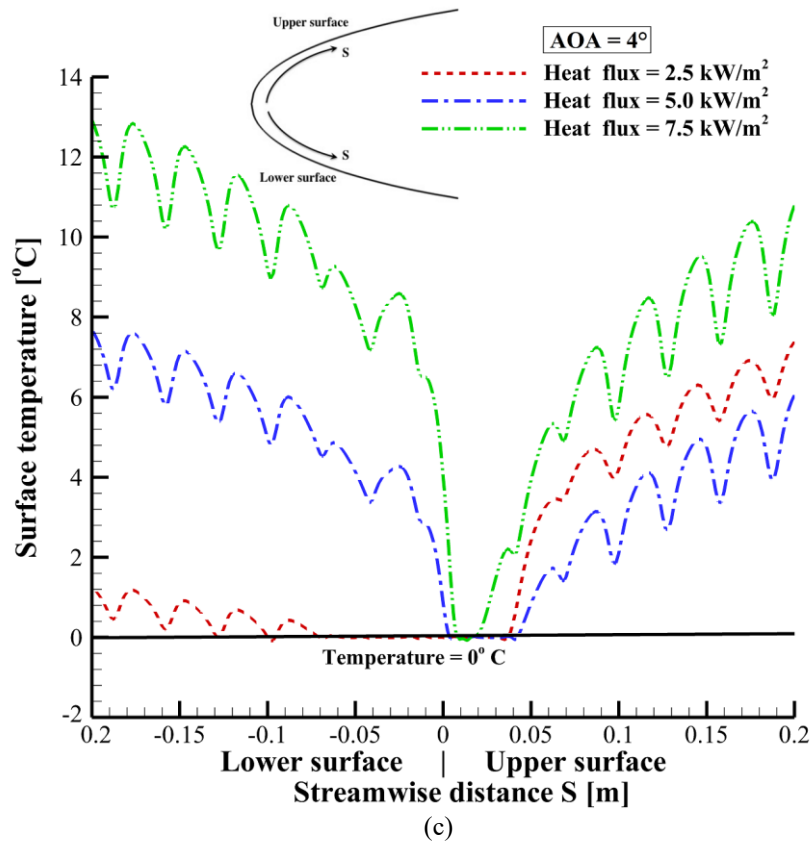
Streamwise distance S [m]

Figure 14: Multiphysics simulation results for the 15-heater IPS airfoil: (a) airfoil section temperature contours in the IPS region; (b) airfoil surface temperature for AOA = 0°; (c) airfoil surface temperature for AOA = 4°.

The airfoil surface temperature results in Fig. 14(c) also reflect a cooler lower surface for a heat flux of 2.5 kW/m², although the lower surface is slightly hotter for heat fluxes of 5.0 kW/m² and 7.5 kW/m². This can be explained by the local airflow velocity over the surfaces, which depends on the airfoil AOA as usual, but here also depends on the disturbance caused by the accreted ice. Increased airflow velocity generally favors increased convective cooling, due to increased air mass inflow. It can be seen in the simulation results in Fig. 12 for {AOA = 4°} that the accreted "ice horn" at 2.5 kW/m² heat flux generated zones of lower airflow velocities over the upper surface (blue color). This effect was diminished for 5.0 kW/m² heat flux, and for the 7.5 kW/m² heat flux the airflow velocity was markedly higher over the clean upper airfoil surface (red color).

Figures 13(b)–13(c) show a pronounced drop in the airfoil surface temperature in the spacing gaps areas for the 5 heater IPS. The temperature there fell to 0°C or below, even with an applied heat flux of 10.0 kW/m². These characteristics were also reflected in the double heating film panel still air thermal response test results, as was shown in Fig. 8(b).

With the 15 heater IPS (Figs. 14(b)–14(c)), the airfoil surface temperature stayed farther above 0°C on the entire leading-edge area, in the range of 0–13°C. This of course follows from the overall higher applied heat flux (15 heaters versus 5 heaters). This temperature range emphasizes the advantage of using heating zones and heat flux modulation, as the heat flux can be reduced in zones where the temperature is in the upper part of the range. The temperature drop in the spacing gap areas is now lower at around 2–3°C, which represents a steadier temperature distribution and lessens the possibility of runback ice formation. Looking at Fig. 14(c) in the case of 4° AOA, it appears that convective cooling would generally be slightly greater on the upper surface of a clean anti-iced airfoil since the resulting surface temperature is relatively lower there compared to the lower surface (heat fluxes of 5.0 and 7.5 kW/m²). This may suggest a favorable IPS design with slightly more power on the upper airfoil surface, since a fixed-wing aircraft normally operates with a positive AOA.

As discussed earlier, the relatively low thermal conductivity of CFRP composites is the main reason for the drop in temperature between heating film units. Furthermore, the temperature drop in wet dynamic air conditions is expected to be more significant than dry still air test conditions, because of the higher convective cooling and added evaporative cooling. It is therefore advantageous to reduce the spacing gap distance to a minimum and ensure that the resistive heating element of the film extends as close as possible to the ends of its sides (see Fig. 3 (b)). It is also still good to have gaps or sectors to apply potentially energy-saving modulated zone heating. A further study to determine an optimal location of the heating films could make use of formal optimization methods [61–64]. If we consider the 15 heaters IPS applied over a wingspan of 6 meters and suppose using 30 meters of electrical wires, the added IPS component mass is estimated at 1.16 kg; this compares to the group 3 UAV weight range of 25–600 kg. The total power required to ensure anti-icing, considering a uniform heat flux of 7.5 kW/m^2, would be 16.9 kW.

Looking at Figs. 14(b)–14(c) for the case with 7.5 kW/m^2 heat flux, each local peak in the surface temperature curve corresponds approximately to the centerline location of a heating film unit. Modulating the heat flux of individual heating film units could potentially generate a more even temperature distribution. Here the existing heating zone resolution length of 27 mm (one heating film width plus one gap length) appears to be enough to do so; this zone length represents a chord length fraction of 0.027. This consideration highlights the importance and complexity of multiphysics simulation for proper IPS design in atmospheric icing conditions. For every different flight condition (airspeed, altitude, angle of attack), icing condition (water droplet size, liquid water content, air temperature), and wing airfoil geometry, the optimal strategy to melt accreted ice will vary [65–68]. This application may therefore lead itself to a formal study of uncertainty or stochastic system load identification [69].

4. Conclusion

We investigated a case application of an electrothermal ice protection system (IPS) integrated into the CFRP laminate wing leading edge of a UAV aircraft. We conducted a preliminary sizing calculation of the required heating film power capacity rating using a simplified one-dimensional heat transfer analysis. A series of CFRP laminate panels with embedded electrothermal heating films were fabricated and their thermal response was tested. These tests were also modeled with the FEM, and the simulation results were in agreement with surface temperature test measurement results to within a 1.54°C difference for all panels considered. This simple thermal FEM simulation was useful for design purposes related to material selection and system configuration. It was evident that the presence of an aluminum foil erosion shield greatly improved spatial heat conduction since the thermal conductivity coefficient of aluminum is much greater than CFRP. FEM was also used for a design study where the heating films were placed closer to the outside surface, but under a thin aluminum foil. Results showed that this configuration would provide a net thermal advantage.

A selected CFRP-based IPS laminate configuration was modeled in the multiphysics icing simulation of a UAV aircraft wing airfoil. Two IPS designs were considered, with 5 or 15 heating film units in the leading-edge area. The simulation considered representative glaze ice conditions for such aircraft. Model parameters varied for each IPS design, and included the airfoil angle of attack and the heating film heat flux level. The results showed that an attainable film heat flux of 7.5 kW/m^2 can achieve full anti-icing functionality with the 15 heating film IPS design. The corresponding anti-icing airfoil surface temperature distribution was in the range of 0–13°C, and in general, the temperature was higher with increasing distance from the leading edge. When an angle of attack of 4° was used, the resulting airfoil surface temperature distribution was asymmetric with relatively cooler temperatures on the upper surface. Multiphysics simulation also captured the formation of runback ice, and this phenomenon was more prevalent for the 5 heater IPS design. Graphical displays of the simulated airfoil surface temperature indicated that an uneven temperature distribution can promote runback ice formation. This is a point of attention for CFRP-based IPS, since their inherently low thermal conductivity is more prone to generating a fluctuating surface temperature distribution.

This study provides insights on the heat flux level necessary to achieve anti-icing, and the corresponding surface temperature distribution, and the effect of heater units positioning. The determined surface temperature range confirms the advantages of using

heating zones and modulating heat flux; the heat flux can be reduced in zones where the resulting surface temperature is relatively higher than elsewhere. This can be the subject of a further study, with the goal of pre-determining heater modulation laws to improve power consumption efficiency while ensuring anti-icing functionality.

Acknowledgements

Appendix: One-dimensional heat transfer analysis

Referring to Fig. A.1, the heat transfer balance in the thickness direction is determined first, considering heat flux generated from the heating film (q''_c) and the heat flux through the surfaces (q''_1 and q''_2) (equation A.1). The heat flux from the heating film to the surfaces is detailed as in equation A.2, where T_c is the heating film temperature, $T_{\infty 1}$ and $T_{\infty 2}$ are the ambient temperatures outside the surfaces, $R''_{t,c}$ is the heating film/CFRP interface resistance, k_{CFRP} is the CFRP thermal conductivity in the thickness direction, l_1 and l_2 are the CFRP thicknesses on each side of the heating film, and h_1 and h_2 are the total surface heat transfer coefficients. The heat flux through the outside surface (q''_1) can be simply expressed by considering the surface temperature difference ($T_1 - T_{\infty 1}$) (equation A.3), which enables the exposed surface temperature T_1 to be expressed (equation A.4).

$$q''_c = q''_1 + q''_2 \tag{A.1}$$

$$q''_c = \frac{T_c - T_{\infty 1}}{R''_{t,c} + \frac{l_1}{k_{CFRP}} + \frac{1}{h_1}} + \frac{T_c - T_{\infty 2}}{R''_{t,c} + \frac{l_2}{k_{CFRP}} + \frac{1}{h_2}} \tag{A.2}$$

$$q''_1 = h_1 (T_1 - T_{\infty 1}) \tag{A.3}$$

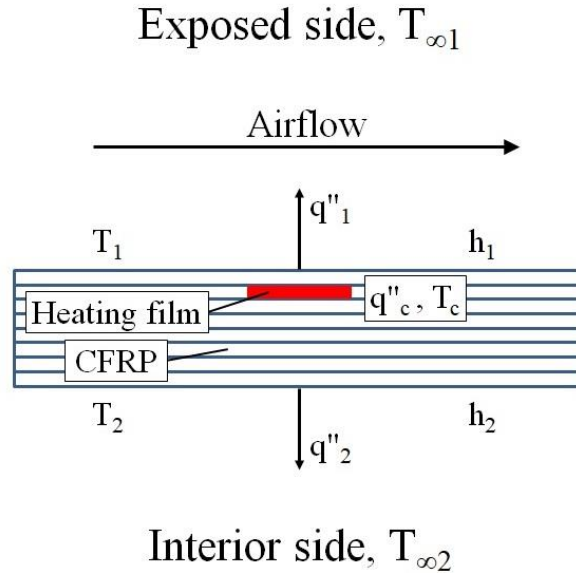$$T_1 = T_{\infty 1} + \frac{q''_1}{h_1} \tag{A.4}$$

Figure A.1: Schematic layout of the CFRP laminate with integrated heating film for the 1D heat transfer analysis.

Let us first assume a turbulent transition Reynolds number (Re_x) of 5×10^5 [39]. With the definition of the Reynolds number in equations A.5, where μ is the air dynamic viscosity, ρ is the air density, and υ is the air velocity, we determine a turbulent transition location (x) at 0.072 meter from the leading edge. It is thus expected that the IPS will be next to both laminar and turbulent flows. For

the laminar portion, we determine the thermal diffusivity of air (α) with equation A.6, where k is the air thermal conductivity and C_p is the air specific heat capacity. Next, the dimensionless Prandtl number (P_r) is calculated with equation A.7, leading to calculate an average Nusselt number ($\overline{Nu_x}$) with the empirical correlation represented in equation A.8. An average laminar surface heat transfer coefficient ($\bar{h}_{lam}$) is deducted from the definition of the average Nusselt number (equation A.9). For the turbulent portion, we chose to calculate the Reynolds number at a conservative distance of 0.3 meter ($Re_{0.3}$) with equation A.10, and then calculate the corresponding Nusselt number ($Nu_{0.3}$) using the empirical correlation of equation A.11. A turbulent surface heat transfer coefficient ($h_{0.3}$) is obtained from the Nusselt number definition (equation A.12). With the calculated surface heat transfer coefficients, and if we take $T_{\infty 1} = T_{\infty 2} = T_\infty$, it is now possible to solve equation A.2 to obtain the required heat flux q''_c to generate the desired heating film temperature T_c of 70°C. Details of the calculation for each airflow condition are presented in Table A.1.

$$x = \frac{\mu Re_x}{\rho v} = \frac{1.469 \times 10^{-5} \cdot 5 \times 10^5}{0.7885 \cdot 128.6} = 0.072 \text{ m} \tag{A.5}$$

$$\alpha = \frac{k}{\rho C_p} = \frac{0.0225}{0.7885 \cdot 1005} = 2.839 \times 10^{-5} \left[\frac{\text{m}^2}{\text{sec.}}\right] \tag{A.6}$$

$$Pr = \frac{\mu}{\rho \alpha} = \frac{1.469 \times 10^{-5}}{0.7885 \cdot 2.839 \times 10^{-5}} = 0.656 \tag{A.7}$$

$$\overline{Nu_x} = 0.664 \cdot Re^{1/2} \cdot Pr^{1/3} = 0.664 \cdot (5 \times 10^5)^{1/2} \cdot 0.656^{1/3} = 408.0 \tag{A.8}$$

$$\bar{h}_{lam} = \frac{\overline{Nu_x} \cdot k}{x} = \frac{408.0 \cdot 0.0225}{0.072} = 127 \left[\frac{\text{W}}{\text{m}^2 \cdot {}^\circ\text{C}}\right] \tag{A.9}$$

$$Re_{0.3} = \frac{\rho v \cdot 0.3}{\mu} = \frac{0.7885 \cdot 128.6 \cdot 0.3}{1.469 \times 10^{-5}} = 2.07 \times 10^6 \tag{A.10}$$

$$Nu_{0.3} = 0.0296 \cdot R_{0.3}^{4/5} \cdot Pr^{1/3} = 0.0296 \cdot (2.07 \times 10^6)^{4/5} \cdot 0.656^{1/3} = 2906 \tag{A.11}$$

$$h_{0.3} = \frac{Nu_{0.3} \cdot k}{0.3} = \frac{2906 \cdot 0.0225}{0.3} = 218 \left[\frac{\text{W}}{\text{m}^2 \cdot {}^\circ\text{C}}\right] \tag{A.12}$$

Table A.1: Calculation details for one-dimensional heat transfer analysis.

Airflow condition:	Still air	Laminar flow	Turbulent flow
T_∞ [°C]	-40	-55	-55
$R''_{t,c}$ [m²·K/W]	5.5E-05	5.5E-05	5.5E-05
l_1 [mm]	0.12	0.12	0.12
l_2 [mm]	0.72	0.72	0.72
h_1 [W/(m²·K)]	5	127	218
h_2 [W/(m²·K)]	5	5	5
q''_c [kW/m²]	1.10	16.11	26.83
q''_1 [kW/m²]	0.55	15.49	26.21
T_1 [°C]	69.9	67.2	65.2

References

[1] Prince Raj L, Lee JW, Myong RS. Ice accretion and aerodynamic effects on a multi-element airfoil under SLD icing conditions. Aerosp Sci Technol 2019;85:320–33. https://doi.org/10.1016/j.ast.2018.12.017.

[2] Federal Aviation Regulations. Part 25 - Airworthiness standards: transport category airplanes. Fed Aviat Adm (FAA), USA 1989:86.

[3] BEA. Final report on the accident on 1st June 2009 to the Airbus A330-203 registered F-GZCP operated by Air France flight AF 447 Rio de Janeiro – Paris. Paris: 2012.

[4] European Aviation Safety Agency. Certification specifications and acceptable means of compliance for large aeroplanes. 2020.

[5] Aubert R. Rotorcraft in-flight icing, Lecture 9. Simulation Methods Used for the In-flight Icing Certification of Aircraft, Rotorcraft and Jet Engines, Fort Worth: Bell Helicopter; 2013.

[6] Lammers K, Van't Hoff S, Ferschitz H, Wannemacher M. Helicopter engine air intake icing wind tunnel certification test. 44th Eur Rotorcr

Forum 2018, ERF 2018 2018;2:1280–9.

[7] Ahn GB, Jung KY, Myong RS, Shin HB, Habashi WG. Numerical and experimental investigation of ice accretion on rotorcraft engine air intake. J Aircr 2015;52:903–9. https://doi.org/10.2514/1.C032839.

[8] ANSYS FENSAP-ICE tutorial guide. Canonsburg: ANSYS, Inc.; 2019.

[9] Goraj Z. An overview of the de-icing and anti-icing technologies with prospects for the future. 24th Int Congr Aeronaut Sci 2004:1–11.

[10] Meier O, Scholz D. A handbook method for the estimation of power de-icing systems. Ger. Aerosp. Congr. 2010, 2010, p. 1–18.

[11] Alemour B, Badran O, Hassan MR. A review of using conductive composite materials in solving lightening strike and ice accumulation problems in aviation. J Aerosp Technol Manag 2019;11:1–23. https://doi.org/10.5028/jatm.v11.1022.

[12] Yao X, Hawkins SC, Falzon BG. An advanced anti-icing/de-icing system utilizing highly aligned carbon nanotube webs. Carbon 2018;136:130–8. https://doi.org/10.1016/j.carbon.2018.04.039.

[13] Endres M, Sommerwerk H, Mendig C, Sinapius M, Horst P. Experimental study of two electro-mechanical de-icing systems applied on a wing section tested in an icing wind tunnel. CEAS Aeronaut J 2017;8:429–39. https://doi.org/10.1007/s13272-017-0249-0.

[14] Venna S V., Lin YJ, Botura G. Piezoelectric transducer actuated leading edge de-icing with simultaneous shear and impulse forces. J Aircr 2007;44:509–15. https://doi.org/10.2514/1.23996.

[15] Strobl T, Storm S, Thompson D, Hornung M, Thielecke F. Feasibility study of a hybrid ice protection system. J Aircr 2015;52:2064–76. https://doi.org/10.2514/1.C033161.

[16] Kim T, Chung DDL. Carbon fiber mats as resistive heating elements. Carbon 2003;41:2436–40. https://doi.org/10.1016/S0008-6223(03)00288-4.

[17] Zhang Z, Chen B, Lu C, Wu H, Wu H, Jiang S, et al. A novel thermo-mechanical anti-icing/de-icing system using bi-stable laminate composite structures with superhydrophobic surface. Compos Struct 2017;180:933–43. https://doi.org/10.1016/j.compstruct.2017.08.068.

[18] De Rosa F, Esposito A. Electrically heated composite leading edges for aircraft anti-icing applications. Fluid Dyn Mater Process 2012;8:107–28. https://doi.org/10.3970/fdmp.2011.008.107.pdf.

[19] Mohseni M, Amirfazli A. A novel electro-thermal anti-icing system for fiber-reinforced polymer composite airfoils. Cold Reg Sci Technol 2013;87:47–58. https://doi.org/10.1016/j.coldregions.2012.12.003.

[20] Chu H, Zhang Z, Liu Y, Leng J. Self-heating fiber reinforced polymer composite using meso/macropore carbon nanotube paper and its application in deicing. Carbon 2014;66:154–63. https://doi.org/10.1016/j.carbon.2013.08.053.

[21] Falzon BG, Robinson P, Frenz S, Gilbert B. Development and evaluation of a novel integrated anti-icing/de-icing technology for carbon fibre composite aerostructures using an electro-conductive textile. Compos Part A Appl Sci Manuf 2015;68:323–35. https://doi.org/10.1016/j.compositesa.2014.10.023.

[22] Kim M, Sung DH, Kong K, Kim N, Kim BJ, Park HW, et al. Characterization of resistive heating and thermoelectric behavior of discontinuous carbon fiber-epoxy composites. Compos Part B Eng 2016;90:37–44. https://doi.org/10.1016/j.compositesb.2015.11.037.

[23] Glover ENK, Bowen CR, Gathercole N, Pountney O, Ball M, Spacie C, et al. Graphene based skins on thermally responsive composites for deicing applications. Behav Mech Multifunct Mater Compos 2017 2017;10165:101650G. https://doi.org/10.1117/12.2260069.

[24] Laroche A. Comparative evaluation of embedded heating elements as electrothermal ice protection systems for composite structures. Concordia University, 2017.

[25] Karim N, Zhang M, Afroj S, Koncherry V, Potluri P, Novoselov KS. Graphene-based surface heater for de-icing applications. RSC Adv 2018;8:16815–23. https://doi.org/10.1039/c8ra02567c.

[26] Zhao Z, Chen H, Liu X, Liu H, Zhang D. Development of high-efficient synthetic electric heating coating for anti-icing/de-icing. Surf Coatings Technol 2018;349:340–6. https://doi.org/10.1016/j.surfcoat.2018.06.011.

[27] Liu X, Chen H, Zhao Z, Yan Y, Zhang D. Slippery liquid-infused porous electric heating coating for anti-icing and de-icing applications. Surf Coatings Technol 2019;374:889–96. https://doi.org/10.1016/j.surfcoat.2019.06.077.

[28] Ibrahim Y, Kempers R, Amirfazli A. 3D printed electro-thermal anti- or de-icing system for composite panels. Cold Reg Sci Technol 2019;166:102844. https://doi.org/10.1016/j.coldregions.2019.102844.

[29] Jeck RK. Icing design envelopes (14 CFR parts 25 and 29, appendix C) converted to a distance-based format. Washington, DC: U.S. Department of Transportation, Federal Aviation Administration; 2002.

[30] Mu Z, Lin G, Shen X, Bu X, Zhou Y. Numerical simulation of unsteady conjugate heat transfer of electrothermal deicing process. Int J Aerosp Eng 2018;2018. https://doi.org/10.1155/2018/5362541.

[31] UAS task force, airspace integration integrated product team. Unmanned aircraft system airspace integration plan. Department of Defense, United States of America; 2011.

[32] SKYFLEX prepreg: materials selection guide. Seongnam, South Korea: SK Chemicals; 2014.

[33] Park SS, Choe HS, Kwak BS, Choi JH, Kweon JH. Micro-bolt repair for delaminated composite plate under compression. Compos Struct 2018;192:245–54. https://doi.org/10.1016/j.compstruct.2018.02.087.

[34] Davies DP, Jenkins SL. Mechanical and metallurgical characterisation of electroformed nickel for helicopter erosion shield applications. Mater Sci Eng A 2014;607:341–50. https://doi.org/10.1016/j.msea.2014.03.122.

[35] LOCTITE EA 9394 AERO epoxy paste adhesive. Bay Point, USA: Henkel Corporation Aerospace; 2013.

[36] Pilling MW, Yates B, Black MA, Tattersall P. The thermal conductivity of carbon fibre-reinforced composites. J Mater Sci 1979;14:1326–38. https://doi.org/10.1007/BF00549304.

[37] Hubbard JA, Brown AL, Dodd AB, Gomez-vasquez S, Ramirez CJ. Carbon fiber composite characterization in adverse thermal environments. Albuquerque: Sandia National Laboratories; 2011.

[38] MatWeb material property data, 2019. www.matweb.com (accessed October 1, 2019).

[39] Incropera FP, DeWitt DP. Fundamentals of heat and mass transfer. 4th ed. New York: John Wiley & Sons; 1996.

[40] Gosse J, Gray WA. Technical guide to thermal processes. Cambridge: Cambridge University Press; 1986.

[41] Barreca F, Fichera CR. Thermal insulating characteristics of cork agglomerate panels in sustainable food buildings. CEUR Workshop Proc., vol. 1498, 2015, p. 358–66.

[42] Dupont Kapton®: summary of properties. DuPont de Nemours, Inc. 2017.

[43] Bejan A. Advanced engineering thermodynamics. 2nd ed. New York: John Wiley & Sons; 1997. https://doi.org/10.1080/03043799808928263.

[44] Li L, Liu Y, Zhang Z, Hu H. Effects of thermal conductivity of airframe substrate on the dynamic ice accretion process pertinent to UAS inflight icing phenomena. Int J Heat Mass Transf 2019;131:1184–95. https://doi.org/10.1016/j.ijheatmasstransfer.2018.11.132.

[45] Chauvin R, Bennani L, Trontin P, Villedieu P. An implicit time marching Galerkin method for the simulation of icing phenomena with a triple layer model. Finite Elem Anal Des 2018;150:20–33. https://doi.org/10.1016/j.finel.2018.07.003.

[46] Breuer UP. Commercial aircraft composite technology. Cham: Springer International Publishing; 2016. https://doi.org/10.1007/978-3-319-31918-6.

[47] Pham QT. Food freezing and thawing calculations. New York: Springer-Verlag; 2014. https://doi.org/10.1007/978-1-4939-0557-7.

[48] Sugimoto E. Applications of polyimide films to the electrical and electronic industries in Japan. IEEE Electr Insul Mag 1989;5:15–23. https://doi.org/10.1109/57.16949.

[49] Rapolu K, Dugan S, Manelis M, Weldon J, Wessel R. Kapton RS flexible heaters - Design and applications. Proc. 17th Intersoc. Conf. Therm. Thermomechanical Phenom. Electron. Syst., San Diego, CA, USA: IEEE; 2018, p. 19–25. https://doi.org/10.1109/ITHERM.2018.8419521.

[50] Chu K, Yun DJ, Kim D, Park H, Park SH. Study of electric heating effects on carbon nanotube polymer composites. Org Electron 2014;15:2734–41. https://doi.org/10.1016/j.orgel.2014.07.043.

[51] Cao Y, Farha FI, Ge D, Liu X, Liu W, Li G, et al. Highly effective e-heating performance of nickel coated carbon fiber and its composites for de-icing application. Compos Struct 2019;229:111397. https://doi.org/10.1016/j.compstruct.2019.111397.

[52] Wu T, Zhou G, Cai D, Zhou F, Cai L. Effect of internal heating on delamination properties of deicing composite curved beams under four-point bending. Compos Struct 2021;256:113084. https://doi.org/10.1016/j.compstruct.2020.113084.

[53] Rizzo F, Pinto F, Meo M. Development of multifunctional hybrid metal/carbon composite structures. Compos Struct 2019;222:110907. https://doi.org/10.1016/j.compstruct.2019.110907.

[54] Bouhamed A, Kia AM, Naifar S, Dzhagan V, Müller C, Zahn DRT, et al. Tuning the adhesion between polyimide substrate and MWCNTs/epoxy nanocomposite by surface treatment. Appl Surf Sci 2017;422:420–9. https://doi.org/10.1016/j.apsusc.2017.05.177.

[55] Harman AB, Wang CH. Improved design methods for scarf repairs to highly strained composite aircraft structure. Compos Struct 2006;75:132–44. https://doi.org/10.1016/j.compstruct.2006.04.091.

[56] Kulkarni MR, Brady RP. A model of global thermal conductivity in laminated carbon/carbon composites. Compos Sci Technol 1997;57:277–85. https://doi.org/10.1016/S0266-3538(96)00116-9.

[57] Beaugendre H, Morency F, Habashi WG. FENSAP-ICE's three-dimensional in-flight ice accretion module: ICE3D. J Aircr 2003;40:239–47. https://doi.org/10.2514/2.3113.

[58] Jung SK. A computational modeling for semi-coupled multiphase flow in atmospheric icing conditions. J Aerosp Technol Manag 2015;7:351–64. https://doi.org/10.5028/jatm.v7i3.499.

[59] Croce G, Beaugendre H, Habashi WG. Numerical simulation of heat transfer in mist flow. Numer Heat Transf Part A Appl 2002;42:139–52. https://doi.org/10.1080/10407780290059477.

[60] Prince Raj L, Yee K, Myong RS. Sensitivity of ice accretion and aerodynamic performance degradation to critical physical and modeling parameters affecting airfoil icing. Aerosp Sci Technol 2020;98:105659. https://doi.org/10.1016/j.ast.2019.105659.

[61] Yang C, Hou X, Chang S. A synchronous placement and size-based multi-objective optimization method for heat dissipation design on antenna module of space solar power satellite. Sustain Energy Technol Assess 2021;45:101183. https://doi.org/10.1016/j.seta.2021.101183.

[62] Yang C. An adaptive sensor placement algorithm for structural health monitoring based on multi-objective iterative optimization using weight factor updating. Mech Syst Signal Process 2021;151:107363. https://doi.org/10.1016/j.ymssp.2020.107363.

[63] Yang C, Liang K, Zhang X. Strategy for sensor number determination and placement optimization with incomplete information based on interval possibility model and clustering avoidance distribution index. Comput Methods Appl Mech Eng 2020;366:113042. https://doi.org/10.1016/j.cma.2020.113042.

[64] Yang C, Liang K, Zhang X, Geng X. Sensor placement algorithm for structural health monitoring with redundancy elimination model based on sub-clustering strategy. Mech Syst Signal Process 2019;124:369–87. https://doi.org/10.1016/j.ymssp.2019.01.057.

[65] Pourbagian M, Habashi WG. Surrogate-based optimization of electrothermal wing anti-icing systems. J Aircr 2013;50:1555–63. https://doi.org/10.2514/1.C032072.

[66] Raj LP, Jeong H, Roy R, Kweon JH, Myong RS. Computational simulation of an electrically heated ice protection system for composite leading edges of aircraft. SAE Tech. Pap. 2019-01-2041, SAE International; 2019. https://doi.org/10.4271/2019-01-2041.

[67] Pourbagian M, Habashi WG. Aero-thermal optimization of in-flight electro-thermal ice protection systems in transient de-icing mode. Int J Heat Fluid Flow 2015;54:167–82. https://doi.org/10.1016/j.ijheatfluidflow.2015.05.012.

[68] Jung SK, Raj LP, Rahimi A, Jeong H, Myong RS. Performance evaluation of electrothermal anti-icing systems for a rotorcraft engine air intake using a meta model. Aerosp Sci Technol 2020;106. https://doi.org/10.1016/j.ast.2020.106174.

[69] Yang C. A novel uncertainty-oriented regularization method for load identification. Mech Syst Signal Process 2021;158:107774. https://doi.org/10.1016/j.ymssp.2021.107774.